Acta Astronautica 216 (2024) 214–228

Contents lists available at ScienceDirect

Acta Astronautica

journal homepage: www.elsevier.com/locate/actaastro

Research paper

Modeling, simulation and control of a spacecraft: Automated reorientation under directional constraints

Simone Fiori [a,*], Luca Sabatini [b], Francesco Rachiglia [c], Edoardo Sampaolesi [d]

[a] Departement of Information Engineering, Marches Polytechnic University, Via Brecce Bianche, Ancona, 60131, Italy
[b] School of Automation Engineering, University of Bologna, Via Zamboni, 33, Bologna, 40122, Italy
[c] School of Robotics Engineering, University of Genoa, Viale Causa, 13, Genova, 16145, Italy
[d] School of Space and Astronautical Engineering, University "La Sapienza" of Rome, Via Eudossiana, 18, Rome, 00184, Italy

ARTICLE INFO

Keywords:
Lie-group theory
Reorientation maneuver
Spacecraft
Space station

ABSTRACT

The aim of the present research endeavor is to propose a framework to model, simulate and control the reorientation of an exploration-class spacecraft for space observation operations. Reorientation under boresight evasion requirements will be tackled by a virtual-potential theory which encodes a reorientation target as well as mandatory-direction-type and forbidden-direction-type attitudinal constraints. The mathematical model of the rotational motion of a spacecraft as well as the control fields are entirely written by coordinate-free Lie-group-type formulations. Numerical simulations complement the theoretical endeavor and illustrate the achieved progress.

1. Introduction

Autonomous guidance of small-sized unmanned spacecrafts has been a goal in aerospace research since the inception of space missions. Autonomous guidance is able to overcome communications delays with the ground mission guidance station while benefiting from direct on-site obstacle sensing and avoidance. In addition, autonomous guidance may help in mitigating accidents due to human errors that are always lurking. A recent example is the accident occurred to the Voyager 2 spacecraft, already about 12.4 billion miles away, that lost contact to the base station at the end of July 2023, when flight commanders accidentally pinged across an incorrect command that caused it to tilt its antenna away from Earth (full communication was re-established at the beginning of August 2023) [1]. Current and future orbital missions involve operations in the proximity of large space structures, such as the International Space Station [2], the most prominent of which are *autonomous rendezvous* and *reorientation*.

Reorientation of a spacecraft is a fundamental operation to be carried out during an exploratory mission. Large-angle attitude slew maneuvers are required to achieve re-targeting of payload instrumentation during science missions [3], while in orbit around the Earth. Reorientation from one direction to another must be operated in such a way that the boresight of sensitive instrumentation, such as cryogenically cooled infrared telescopes [3] and star sensors [4], is not directed toward any bright object such as the sun, the Earth or the moon, while the radio antenna does not loose communication with the ground or the space station [5]. In particular, boresight evasion entails the notion of attitude forbidden constraints [4]. Automated reorientation in the presence of attitude constraints poses a challenging computational task for the on-board guidance control system [6].

The mathematical representation to model the roto-translational dynamics of a spacecraft, as well as the control strategy to make a spacecraft execute the necessary movements in space, are a subject of continued debate in the scientific community. In particular, the mathematical representation of the rotational dynamics may be picked from the realms of Tait–Bryan representation, quaternions and rotation matrices. Tait–Bryan angles carry an intuitive and easy-to-visualize value [7], although the conversion from angular to Cartesian coordinate is burdened by complex trigonometric expressions and from inherent singularities [6]. Quaternion-based representations are often invoked in aerospace engineering [6], although quaternions are affected by the well-known problem of unwinding due to the redundancy of the unit quaternion (namely, when the rotation angle is sufficiently large, the trajectory of attitude maneuver may be longer, leading to increased propellant consumption and longer maneuver time) [4]. In addition, in the present authors' opinion, quaternion machinery results in unnecessarily complicated expressions that directly affect modeling as well control design. Albeit inherently redundant, coordinate-free rotation-matrices representations result to be singularity free [8] and

* Corresponding author.
E-mail address: s.fiori@staff.univpm.it (S. Fiori).
URL: http://web.dii.univpm.it/fiori (S. Fiori).

https://doi.org/10.1016/j.actaastro.2023.12.053
Received 21 June 2023; Received in revised form 15 October 2023; Accepted 26 December 2023
Available online 5 January 2024

easy to manage in modeling and control design thanks to the underlying theory of Lie groups [9–11], hence rotation-matrices representations are the mathematical tool of choice in the present research endeavor.

Automated control of rigid bodies, such as drones, satellites, ground robots as well as remotely operated underwater vehicles, may benefit from the theory of virtual attractive–repulsive potentials, which has been explored and extended across decades [12–17]. Artificial-potential-based control relies on artificial potential functions constructed so as to assign a potential value to each point of the state space in a way that promotes state transition toward a set goal while demoting state transitions toward obstructions. As specific references for the present endeavor, we cite the paper [18] that revises and utilizes gradient-based control fields in conjunction with further physically-plausible forces, the paper by the present first author and co-workers [19], that extended the theory of virtual attractive–repulsive potential to control rotational dynamics by Lie-group theory, and the paper [6] that introduced the notion of barrier-type potentials to control the attitudinal dynamics of a spacecraft (in quaternion representation).

After recalling the principal equations governing the motion of an orbital spacecraft, we shall present a control strategy to effect reorientation under mandatory/forbidden directional constraints. A distinguishing feature of the present research endeavor is that attitudes are represented through orthogonal rotation matrices and that the corresponding control actions are represented through vector fields on the space of skew-symmetric matrices. Such kind of matrices are treated as a whole, without any need to resort to angular coordinates nor scalar velocities. Albeit, as a matter of fact, it is difficult for engineers and practitioners to free themselves from the need to make use of scalar variables, the present paper, among others, shows that it is, in fact, convenient to abandon coordinates-based representations in favor of a modern, high-level computing-oriented, compact representation. A relation between quaternion and rotation-matrix representations is briefly discussed in the Appendix A.

The present document is organized as follows. Section 2 recalls necessary details from orbital dynamics, including the set of reference frames used to describe the equations of rotational motion and the kinds of propulsion systems available within a small-sized spacecraft to modify its attitude. Section 3 details the notion of spacecraft reorientation under directional constraints, with special emphasis on mandatory and forbidden cones of the celestial sphere. In this section, appropriate virtual attractive–repulsive potentials to achieve reorientation are presented along with related gradient-type control torque terms. Section 4 illustrates the theoretical content through an extensive series of numerical simulations based on several cases-of-study from the scientific literature. Section 5 concludes the document and suggests a number of possible improvements to the current endeavor to be tackled in future research projects.

2. Reference frames, physical model and equations of motion of a spacecraft

The present section aims at recalling a number of essential details concerning the reference frames used to describe the equations of motion of a small-sized spacecraft, the type of physical actuators that govern such motion and a mathematical model of motion. Within this section, the terminology that shall be used within this document will be summarized as well. In addition, the numerical implementation of the mathematical model of orbital motion on a computing platform for numerical simulations will be given consideration.

2.1. Application scenario and reference frames

The scenario taken into consideration in the present research endeavor involves an exploration-class unmanned *spacecraft*, endowed with a payload sensor (e.g., a telescope) to conduct scientific observations, a communication device (e.g., a radio antenna) to keep in touch with the ground station and/or the main station, and an on-board autonomous control system that is able to provide appropriate navigation and control actions.

In the examined scenario, the spacecraft is supposed to be endowed with a series of *reaction wheels* that serve to control its rotational dynamics [20]. In particular, the spacecraft is assumed to be endowed with three reaction wheels (one per axis) through which it is possible to modulate any sort of active torque. (Special instances of under-actuated systems are studied, e.g., in [21].)

An inertial reference frame $\mathcal{F}_{\mathrm{I}}$ is introduced to describe the direction of bright objects whose direct light exposure should be avoided, such as the sun, the Earth, the moon. The inertial reference frame $\mathcal{F}_{\mathrm{I}}$ is also necessary to specify the direction of a celestial object to be observed by a telescope as well as the boresight of a transmitting antenna located on a ground station. Target attitudes, mandatory and forbidden pointing directions during reorientation maneuvers are referred to the frame $\mathcal{F}_{\mathrm{I}}$.

A spacecraft-fixed reference frame $\mathcal{F}_{\mathrm{C}}$ is introduced as well, which serves to describe its relative orientation and location with respect to the inertial frame $\mathcal{F}_{\mathrm{I}}$. The Cartesian axes of the reference frame $\mathcal{F}_{\mathrm{C}}$ are assumed to be aligned to the principal axes of inertia of the spacecraft. (We shall adopt the axis convention shown in the Figure 7 of the paper [6].) The relative orientation and location enters the control goals to be fulfilled by the spacecraft. To what concerns the rotational dynamics, the spacecraft is considered as a rigid body acted upon by a series of mechanical torques due to the reaction wheels and external disturbances.

The attitude of a spacecraft is quantified by a rotation matrix $R \in \mathrm{SO}(3)$ (namely, a special orthogonal matrix). Such rotation matrix is defined to be the one that aligns the spacecraft-fixed reference frame $\mathcal{F}_{\mathrm{C}}$ to the inertial reference frame $\mathcal{F}_{\mathrm{I}}$. The equations of motion may be derived in a standard minimal-action variational setting which leads to classical Euler–Poincaré equations. Since the spacecraft is subjected to non-conservative torques, such equations are not 'pure' [22].

The rotational dynamics of a rigid body is expressed by a system of two first-order differential equations [9]:

$$\begin{cases} \dot{R} = R\Omega, \;\; R(0) = R_0, \\ \mathbb{J}\dot{\Omega} = \mathbb{Q}\Omega + T_{\mathrm{rw}} + T_{\mathrm{rd}}, \;\; \Omega(0) = \Omega_0, \end{cases} \tag{1}$$

where $\dot{R} \in T_R\mathrm{SO}(3)$ denotes the rotational speed-matrix of the spacecraft, $\Omega \in \mathfrak{so}(3)$ denotes the skew-symmetric angular speed-matrix of the spacecraft, the symbol $\mathbb{J} : \mathfrak{so}(3) \to \mathfrak{so}(3)$ denotes the inertia operator, the operator $\mathbb{Q} : \mathfrak{so}(3) \to \mathfrak{so}(3)$ denotes the resultant of inherent torques due to inertia and mass unbalance within the spacecraft, $T_{\mathrm{rw}} \in \mathfrak{so}(3)$ denotes the mechanical torque exerted by the reaction wheels and $T_{\mathrm{rd}} \in \mathfrak{so}(3)$ denotes a random disturbance term. The quantities $R_0 \in \mathrm{SO}(3)$ and $\Omega_0 \in \mathfrak{so}(3)$ denote initial attitude and angular speed, respectively.

The operator $\mathbb{J}$, which is not a matrix, and the operator $\mathbb{Q}$, stem from the Euler–Poincaré equations of motion on the Lie group SO(3). The function $\mathbb{J}\Omega$ is hence linear (and invertible) in Ω, while the function $\mathbb{Q}\Omega$ is quadratic. As it will be clarified in Section 3, it is not necessary to specify the structure of the operator $\mathbb{Q}$, since a fully-actuated system may be controlled under the principle of dynamics replacement [19], based on inherent dynamics deletion. In the model (1), the second equation establishes the rotational speed in the reference frame $\mathcal{F}_{\mathrm{C}}$. The mechanical torque field T_{rw} will depend on the actual attitude R through the chosen control law. The first equation in the system (1), often referred to as 'reconstruction equation', allows one to reconstruct the actual attitude of the spacecraft in the chosen reference frame.

We remark that, in the present research project, the rotation matrix R is the only quantity that is introduced to represent the attitude of a spacecraft, hence we shall not introduce quaternions nor Euler nor Tait–Bryan angles. In addition, the matrix R will always be treated as a whole, without any needs to resort to its entries or angular coordinates.

Table 1
Summary of the principal mathematical symbols introduced in Section 2.

Symbol	Type	Unit	Meaning
$\mathcal{F}_{\mathrm{I}}$	–	–	Inertial reference frame
$\mathcal{F}_{\mathrm{C}}$	–	–	Spacecraft-fixed reference frame
R	SO(3)	–	Attitude of the spacecraft with respect to $\mathcal{F}_{\mathrm{I}}$
Ω	$\mathfrak{so}(3)$	rad/s	Angular velocity of the spacecraft with respect to $\mathcal{F}_{\mathrm{C}}$
$\mathbb{J}$	$\mathfrak{so}(3) \to \mathfrak{so}(3)$	kg m^2	Inertia operator of the spacecraft
T_{rw}	$\mathfrak{so}(3)$	kg m^2/s^2	Torque exerted on the spacecraft by the internal reaction wheels
T_{rd}	$\mathfrak{so}(3)$	kg m^2/s^2	Random torque representing un-modeled disturbances
T	$\mathfrak{so}(3)$	kg m^2/s^2	Total torque acting on the body of the spacecraft
h	Positive scalar	s	Sampling interval/numerical stepsize

2.2. Numerical implementation of the equations of motion

All in one, the system (1) constitute a system of differential equations on the tangent bundle $T\mathrm{SO}(3)$. To what concerns the numerical integration of the Eqs. (1), it pays to introduce discrete-time counterparts of the involved variables, namely R_s for the attitude matrix, Ω_s for the angular speed matrix, and T_s for the resultant torque matrix $T := T_{\mathrm{rw}} + T_{\mathrm{rd}}$. Then the rotational model (1) may be simulated numerically by the following iteration scheme

$$\begin{cases} R_{s+1} = R_s \mathrm{Exp}(h\,\Omega_s), \\ \Omega_{s+1} = \Omega_s + h\,\mathbb{J}^{-1}(\mathbb{Q}\Omega_s + T_s), \end{cases} \tag{2}$$

where $h > 0$ denotes a numerical stepsize (generally much smaller than 1) measured in seconds (s). We shall notice briefly that the first iteration rule stems from the theory of numerical integration of differential equations on Lie-group bundles. In the above relations, the symbol Exp denotes matrix exponential. Interested readers might find more details in the papers [9,19].

2.3. Summary of the principal symbols introduced in Section 2

Within the present section a number of symbols were introduced, whose type, measurement unit and meaning have been summarized in Table 1.

3. Reorientation under directional constraints

Reorientation is achieved by generating a control action that changes the attitude of the spacecraft from an initial attitude, represented by a rotation matrix $R_{\mathrm{i}} \in \mathrm{SO}(3)$, to a desired attitude, represented by a rotation matrix $R_{\mathrm{d}} \in \mathrm{SO}(3)$. Without any further constraints, the problem would be solved by a *geodesic* motion (namely, the shortest path in the space SO(3)) from R_{i} to R_{d}. In actual space missions, however, reorientation must take into account directional constraints, which may be classified as

- *mandatory directions*, specified by unit vectors $e_{\mathrm{M},i} \in \mathbb{R}^3$ and angular amplitudes $\theta_{\mathrm{M},i}$, that represent cones of amplitude $\theta_{\mathrm{M},i}$ around given directions $e_{\mathrm{M},i} \in \mathbb{R}^3$, that one of the axis of the spacecraft must always lie within, and
- *forbidden directions*, specified by unit vectors $e_{\mathrm{F},i} \in \mathbb{R}^3$ and angular amplitudes $\theta_{\mathrm{F},i}$, that represent cones of amplitude $\theta_{\mathrm{F},i}$ around given directions $e_{\mathrm{F},i} \in \mathbb{R}^3$, that one of the axis of the spacecraft must always keep out from.

An example of mandatory-type constraint arises from the requirement that the boresight of the antenna on the spacecraft keeps within the cone of contact of a ground-station antenna. The angles $\theta_{\mathrm{M},i}$ are generally wider than the angles $\theta_{\mathrm{F},j}$. An example of forbidden-type constraint arises from the necessity to make the boresight of a light-sensitive telescope avoid sunbeams and further bright sources.

The directions $e_{\mathrm{M},i}$ and $e_{\mathrm{F},i}$ are generally specified in the inertial reference frame $\mathcal{F}_{\mathrm{I}}$, while the boresight axes of the antenna, hereafter denoted as e_{BA}, and of the sensor, hereafter denoted as e_{BS}, aboard the spacecraft are specified in the spacecraft-fixed reference frame $\mathcal{F}_{\mathrm{C}}$.

Reorientation is effected via virtual potential functions based on the above information. The novel virtual potential functions defined in the following is based on both an attractive term and on barrier-type repulsive terms and enter the equations of dynamics through their Riemannian gradient.

3.1. Rotational dynamics control by dynamics replacement and a virtual-attractive-repulsive potential

The aim of control design for reorientation purpose is to determine an appropriate control action that affects the rotational dynamics of the spacecraft through Eqs. (1).

The proposed torque-type control field reads

$$T_{\mathrm{rw}} := -\,\mathbb{Q}\Omega - K_{\mathrm{f}}\,\Omega - R^{\top}\nabla_R V, \tag{3}$$

where $V : \mathrm{SO}(3) \to \mathbb{R}$ denotes a virtual attractive–repulsive potential and ∇_R denotes the Riemannian gradient at $R \in \mathrm{SO}(3)$ corresponding to the canonical inner product in the tangent bundle $T\mathrm{SO}(3)$ [23].

The first term on the right-hand side of the relation (3) stems from the principle of dynamics replacement. The purpose of such form of cancellation is to overrule the internal dynamics of a rigid body with the aim of replacing it with a desired dynamics. Such principle may also be referred to as *decoupling* [24].

The second term introduces a sort of rotational braking effect, whose purpose is to slow down the rotational motion and to make the effective control torque less sensitive to excessive control actions. This term, discussed in [4,18,19], also prevents the control algorithm to cause oscillations around the optimal solution, which is a well-known effect in gradient-based optimization. The constant $K_{\mathrm{f}} > 0$ determines the relative importance of such term. In general, dissipative forces proportional to speed are added to promote asymptotic stabilization of a dynamical system [24].

The third term on the right-hand side of the relation (3) provides a torque that drives the attitude of the rigid body toward the minimum of the potential function V. The potential function must be cautiously crafted in such a way to effectively drive the spacecraft from the initial attitude to the desired attitude while avoiding undesired (forbidden) direction and yet meeting favorable (mandatory) inclination. Notice that the potential is defined in the inertial reference frame $\mathcal{F}_{\mathrm{I}}$, and so is its Riemannian gradient $\nabla_R V$, hence it needs to be brought back to the spacecraft-fixed reference frame $\mathcal{F}_{\mathrm{C}}$ before entering the equations by a pre-multiplication by the $\mathcal{F}_{\mathrm{I}}$-to-$\mathcal{F}_{\mathrm{C}}$ reference conversion matrix $R^{\top}$.

On the basis of the chosen control law (3), the angular acceleration of the spacecraft reads

$$\mathbb{J}^{-1}(\mathbb{Q}\Omega + T) = \mathbb{J}^{-1}(-K_{\mathrm{f}}\,\Omega - R^{\top}\nabla_R V + T_{\mathrm{rd}}), \tag{4}$$

hence it does not depend on the internal dynamics anymore. According to literature, the inertia matrix of a spacecraft may be taken diagonal (by an appropriate choice of coordinate system $\mathcal{F}_{\mathrm{C}}$) and even isotropic [6,20]. For the sake of simplification, we shall assume that the three eigenvalues of such matrix take the same value $J_{\mathrm{C}} > 0$, which readily implies that $\mathbb{J}\Omega = J_{\mathrm{C}}\Omega$.

In the following Sections 3.2 and 3.3 we shall present and discuss two different instances of virtual potentials for reorientation purpose, which shall be compared numerically in Section 4.

3.2. Additive potential function and related torque components

As a first attempt to define a potential function, based on an instance of additive–repulsive potential theory developed in [2,6,19], we propose the novel expression

$$V_{\mathrm{ADD}}(R) := A(R) + \sum_i B_i(R), \tag{5}$$

where $A : \mathrm{SO}(3) \to \mathbb{R}$ denotes an attractive potential, whose purpose is to attract the attitude of the spacecraft toward the desired attitude R_{d}, while each $B_i : \mathrm{SO}(3) \to \mathbb{R}$ is a barrier-type repulsive potential aimed at making the spacecraft avoid the forbidden direction while upholding the mandatory directions.

In order to specify the structure of the attractive term, it is necessary to recall the notion of geodesic distance in SO(3) endowed with its canonical metrics [23]. Given two attitudes $R_1, R_2 \in \mathrm{SO}(3)$, their geodesic distance is defined as

$$d(R_1, R_2) := \|\mathrm{Log}(R_1^{\top} R_2)\|_{\mathrm{F}}, \tag{6}$$

where Log denotes the principal matrix logarithm and the symbol $\|\cdot\|_{\mathrm{F}}$ denotes a Frobenius matrix norm.

The attractive potential is defined as a upside-down bell-shaped function of the geodesic distance between the current attitude and the desired attitude as

$$A(R) := -\tfrac{1}{2} K_{\mathrm{A}} \ell^2 \exp\left(-\frac{d^2(R_{\mathrm{d}}, R)}{\ell^2}\right), \tag{7}$$

which appears to be a monotonically increasing function with a minimum in $R = R_{\mathrm{d}}$. The constant $K_{\mathrm{A}} > 0$ determines the absolute strength of this component of the potential, while the constant $\ell > 0$ represents the radius of influence of this component of the potential over the space SO(3): the larger ℓ, the wider its influence area.

In order to compute the Riemannian gradient of the 'attractive' component of the potential, it is worth recalling the golden formula (for a review of manifold calculus in system theory and control, interested readers might consult [23,25]):

$$\nabla_R d^2(R_{\mathrm{d}}, R) = 2\, R\, \mathrm{Log}(R_{\mathrm{d}}^{\top} R). \tag{8}$$

We henceforth get the torque term corresponding to the attractive component of the potential as

$$-R^{\top} \nabla_R A = -K_{\mathrm{A}} \exp\left(-\frac{d^2(R_{\mathrm{d}}, R)}{\ell^2}\right) \mathrm{Log}(R_{\mathrm{d}}^{\top} R). \tag{9}$$

The 'repulsive' component of the potential V_{ADD} is designed to be of barrier type. In the present endeavor, barriers are designed to either keep a given axis of the spacecraft away from forbidden directions or in the angular proximity of a mandatory direction. Let us examine forbidden cones and mandatory cones in details.

Given a mandatory direction $e_{\mathrm{M}} \in \mathbb{R}^3$ expressed in the reference system $\mathcal{F}_{\mathrm{I}}$ and an axis of the spacecraft $e_{\mathrm{BA}} \in \mathbb{R}^3$ expressed in the reference system $\mathcal{F}_{\mathrm{C}}$, the cosine of the angle between these two directions is given by $e_{\mathrm{M}}^{\top} R\, e_{\mathrm{BA}}$, where R denotes the current attitude of the spacecraft with respect to the inertial reference system. In order to make sure that the axis e_{BA} keeps at an angular distance from the mandatory direction e_{M} lesser than a prescribed threshold $0 < \theta_{\mathrm{M}} < \frac{\pi}{2}$, the following constraint needs to be imposed

$$e_{\mathrm{M}}^{\top} R\, e_{\mathrm{BA}} - \cos\theta_{\mathrm{M}} > 0, \tag{10}$$

since the cosine function $\cos(\alpha)$ is decreasing whenever $0 < \alpha \leq \frac{\pi}{2}$. The constraint (10) appears as a *linear inequality* in the attitude matrix R. In this inequality constraint, the angle θ_{M} represents the semi-aperture of the mandatory cone.

A barrier potential to secure adherence to such directional constraint reads

$$B_{\mathrm{M}}(R) := -K_{\mathrm{M}} \log(e_{\mathrm{M}}^{\top} R\, e_{\mathrm{BA}} - \cos\theta_{\mathrm{M}}), \tag{11}$$

where $K_{\mathrm{M}} > 0$ determines the strength of the corresponding torque term in the control action, while the function 'log' denotes natural logarithm. It is immediate to recognize that, as the axis $R\, e_{\mathrm{BA}}$ gets closer to the surface of the mandatory cone, hence the difference $e_{\mathrm{M}}^{\top} R\, e_{\mathrm{BA}} - \cos\theta_{\mathrm{M}}$ approaches 0, the function $B_{\mathrm{M}}(R)$ approaches $+\infty$ hence providing an infinitely steep potential wall (a barrier, in fact).

The above barrier-type virtual potential component is designed to produce an artificial repulsion from the surface of an obstacle, which is represented as the zero sub-level set of a smooth function. The potential component (11), albeit formally different, produces the same effect of the virtual potential introduced in [26], which goes to infinity as the inverse of a known scalar-valued analytic function in the close vicinity of an obstacle and decays to zero at some positive level surface sufficiently far from the obstacle. Such approach is, in turn, based on the obstacle-avoidance technique introduced long before in [24] under the acronym FIRAS (Force Inducing an Artificial Repulsion from a Surface).

The function (11) may equivalently be written as $B_{\mathrm{M}}(R) := -K_{\mathrm{M}} \log(\mathrm{tr}(R\, e_{\mathrm{BA}} e_{\mathrm{M}}^{\top}) - \cos\theta_{\mathrm{M}})$, where symbol 'tr' denotes matrix trace. Now, in order to compute the Riemannian gradient of such matrix-to-scalar function, it pays to recall the formula [23]

$$\nabla_R B = R\sigma\left(R^{\top} \frac{\partial B}{\partial R}\right), \tag{12}$$

where $\sigma : \mathbb{R}^{3\times 3} \to \mathfrak{so}(3)$ is a matrix-to-matrix function defined as $\sigma(Y) := \frac{1}{2}(Y - Y^{\top})$ that represents an orthogonal projection over the space of skew-symmetric matrices, while the symbol $\frac{\partial}{\partial R}$ denotes the ordinary Jacobian. (It is necessary to specify that the expression (12) holds under the assumption that the tangent bundle $T\mathrm{SO}(3)$ is endowed with the canonical inner product $\langle V_1, V_2\rangle_R := \mathrm{tr}(V_1^{\top} V_2)$ for every $V_1, V_2 \in T_R\mathrm{SO}(3)$.)

In the present case, matrix computations reveal that

$$\frac{\partial B_{\mathrm{M}}}{\partial R} = -\frac{K_{\mathrm{M}}}{e_{\mathrm{M}}^{\top} R\, e_{\mathrm{BA}} - \cos\theta_{\mathrm{M}}} e_{\mathrm{M}} e_{\mathrm{BA}}^{\top}, \tag{13}$$

therefore, the torque component corresponding to a mandatory-type barrier potential takes the expression

$$-R^{\top} \nabla_R B_{\mathrm{M}} = \frac{K_{\mathrm{M}}}{e_{\mathrm{M}}^{\top} R\, e_{\mathrm{BA}} - \cos\theta_{\mathrm{M}}} \sigma(R^{\top} e_{\mathrm{M}} e_{\mathrm{BA}}^{\top}). \tag{14}$$

Likewise, given a forbidden direction $e_{\mathrm{F}} \in \mathbb{R}^3$ expressed in the reference system $\mathcal{F}_{\mathrm{I}}$ and an axis of the spacecraft $e_{\mathrm{BS}} \in \mathbb{R}^3$ expressed in the reference system $\mathcal{F}_{\mathrm{C}}$, the cosine of the angle between them is given by $e_{\mathrm{F}}^{\top} R\, e_{\mathrm{BS}}$. In order to make sure that the axis e_{BS} keeps at an angular distance from the mandatory direction e_{F} larger than a prescribed threshold θ_{F}, the following constraint needs to be imposed

$$\cos\theta_{\mathrm{F}} - e_{\mathrm{F}}^{\top} R\, e_{\mathrm{BS}} > 0. \tag{15}$$

(For comparison purpose we recall, e.g. from [4], that such constraint, written on the basis of a quaternion $[q^{\top}\ q_0]^{\top}$ to represent the attitude of a spacecraft, would read

$$\cos\theta_{\mathrm{F}} - (q_0^2 - q^{\top} q) e_{\mathrm{F}}^{\top} e_{\mathrm{BS}} - 2 e_{\mathrm{F}}^{\top} q q^{\top} e_{\mathrm{BS}} - 2 e_{\mathrm{F}}^{\top} q_0 q^{\times} e_{\mathrm{BS}} > 0,$$

where q_0 denotes the real part of the quaternion and the operator $(\cdot)^{\times}$ returns a $\mathfrak{so}(3)$ matrix from a $\mathbb{R}^3$ vector. Notice that we have used the Jet Propulsion Laboratory (JPL) convention to denote quaternions as is customary in the aerospace domain. In contrast to (15), the above nonlinear expression looks cumbersome.)

A barrier potential to secure adherence to such directional constraint reads

$$B_{\mathrm{F}}(R) := -K_{\mathrm{F}} \log(\cos\theta_{\mathrm{F}} - \mathrm{tr}(R\, e_{\mathrm{BS}} e_{\mathrm{F}}^{\top})), \tag{16}$$

where $K_{\mathrm{F}} > 0$ determines the strength of the corresponding torque term in the control action. The torque component corresponding to such a forbidden-type barrier potential takes the expression

$$-R^{\top} \nabla_R B_{\mathrm{F}} = \frac{K_{\mathrm{F}}}{e_{\mathrm{F}}^{\top} R\, e_{\mathrm{BS}} - \cos\theta_{\mathrm{F}}} \sigma(R^{\top} e_{\mathrm{F}} e_{\mathrm{BS}}^{\top}). \tag{17}$$

Gluing all pieces together, the complete additive potential expression reads

$$\begin{aligned} V_{\mathrm{ADD}}(R) = &-\frac{1}{2}K_{\mathrm{A}}\ell^2\exp\left(-\frac{d^2(R_{\mathrm{d}},R)}{\ell^2}\right) \\ &- K_{\mathrm{M}}\sum_i \log(e_{\mathrm{M},i}^{\top}R\,e_{\mathrm{BA}}-\cos\theta_{\mathrm{M},i}) \\ &- K_{\mathrm{F}}\sum_i \log(\cos\theta_{\mathrm{F},i}-e_{\mathrm{F},i}^{\top}R\,e_{\mathrm{BS}}). \end{aligned} \tag{18}$$

The corresponding control torque term $T_{\mathrm{ADD}}(R) := -R^{\top}\nabla_R V_{\mathrm{ADD}}(R)$ reads

$$\begin{aligned} T_{\mathrm{ADD}}(R) = &-K_{\mathrm{A}}\exp\left(-\frac{d^2(R_{\mathrm{d}},R)}{\ell^2}\right)\mathrm{Log}(R_{\mathrm{d}}^{\top}R) \\ &+\sum_i \frac{K_{\mathrm{M}}}{e_{\mathrm{M},i}^{\top}R\,e_{\mathrm{BA}}-\cos\theta_{\mathrm{M},i}}\sigma(R^{\top}e_{\mathrm{M},i}e_{\mathrm{BA}}^{\top}) \\ &+\sum_i \frac{K_{\mathrm{F}}}{e_{\mathrm{F},i}^{\top}R\,e_{\mathrm{BS}}-\cos\theta_{\mathrm{F},i}}\sigma(R^{\top}e_{\mathrm{F},i}e_{\mathrm{BS}}^{\top}), \end{aligned} \tag{19}$$

where summations run over the number of mandatory/forbidden-type constraints, respectively. We have chosen to weight each mandatory-type term with the same constant K_{M} and all forbidden-type terms with the same constant K_{F}, although, in practice, each coefficient may be chosen to take a different value.

It is interesting, and perhaps counter-intuitive, to notice that the torques corresponding to mandatory-type constraints look alike the terms corresponding to forbidden-type constraints. However, the scalar factors in the expression of the former types of constraints are positive-valued, while the scalar factors in the mathematical expression of latter types are negative-valued, hence they behave in an opposite way.

An important aspect to evaluate is the expression of the potential function $\bar{V}_{\mathrm{ADD}} := V_{\mathrm{ADD}}|_{R=R_{\mathrm{d}}}$ and of the corresponding gradient-based torque component $\bar{T}_{\mathrm{ADD}} := -R_{\mathrm{d}}^{\top}[\nabla_R V_{\mathrm{ADD}}]_{R=R_{\mathrm{d}}}$ at the desired attitude. Calculations show that

$$\begin{cases} \bar{V}_{\mathrm{ADD}} &= -\frac{1}{2}K_{\mathrm{A}}\ell^2 - K_{\mathrm{M}}\sum_i \log(e_{\mathrm{M},i}^{\top}R_{\mathrm{d}}\,e_{\mathrm{BA}} \\ &\quad -\cos\theta_{\mathrm{M},i}) - K_{\mathrm{F}}\sum_i \log(\cos\theta_{\mathrm{F},i}-e_{\mathrm{F},i}^{\top}R_{\mathrm{d}}\,e_{\mathrm{BS}}), \\ \bar{T}_{\mathrm{ADD}} &= \sum_i \frac{K_{\mathrm{M}}}{e_{\mathrm{M},i}^{\top}R_{\mathrm{d}}e_{\mathrm{BA}}-\cos\theta_{\mathrm{M},i}}\sigma(R_{\mathrm{d}}^{\top}e_{\mathrm{M},i}e_{\mathrm{BA}}^{\top}) \\ &\quad +\sum_i \frac{K_{\mathrm{F}}}{\cos\theta_{\mathrm{F},i}-e_{\mathrm{F},i}^{\top}R_{\mathrm{d}}e_{\mathrm{BS}}}\sigma(R_{\mathrm{d}}^{\top}e_{\mathrm{F},i}e_{\mathrm{BS}}^{\top}), \end{cases} \tag{20}$$

since $d(R_{\mathrm{d}},R_{\mathrm{d}})=0$ and $\mathrm{Log}(R_{\mathrm{d}}^{\top}R_{\mathrm{d}})=0$. The expression $\bar{V}_{\mathrm{ADD}}$ is useful in numerical simulations to verify as to whether the gradient-based control algorithm seeks in fact for such value of the potential function.

The expression $\bar{T}_{\mathrm{ADD}}$ tells that even at the equilibrium point there exists a non-zero *tidal* torque that tends to orient the spacecraft in a direction that is not exactly the desired one. In formal terms, the solution of the equation $T_{\mathrm{ADD}}(R)=0$ differs from $R=R_{\mathrm{d}}$ because of the residual pull-push effect of the barriers. Such effect is not necessarily disruptive since during reorientation, even if the boresight of a telescope does not match exactly the preferred direction of observation of a target, an observation mission might still be carried out seamlessly.

With the aim of fixing the above-noted inconsistency, in the next section we shall introduce an alternative virtual potential structure.

3.3. Mixed multiplicative-additive potential and related torque components

Scientific literature documents a vast effort in the process of selecting suitable potential functions. While researchers agree that each sub-goal needs to be assigned a specific function (one to represent reorientation goal and one to represent each constraints), existing approaches differ on how to combine such terms to concur in the definition of a virtual potential. To recall a few, the paper [6] suggests a mixed multiplicative/additive potential, where the component associated to re-orientation is multiplied by the sum of the barrier-type components associated to directional obstacles. The paper [4] follows a similar approach, although the components associated to re-orientation and obstacles differ in mathematical structure. The paper [27] remarks that a combination of partial potentials may yield a function bearing multiple critical points and recall the notion of 'navigation functions' which constitute possible remedies to such difficulty. The function proposed in [27] is a nonlinear combination of the reorientation potential and of the sum of the reorientation potential term with the product of constraint-enforcing potentials.

In the present research project, we deemed appropriate to explore the features of a mixed potential inspired by the paper [6]. Such novel mixed potential is a variant of the additive potential (5) and reads

$$V_{\mathrm{MIX}}(R) := A(R) + \frac{1}{2}d^2(R,R_{\mathrm{d}})\sum_i B_i(R), \tag{21}$$

where the attractive sub-potential function A takes the same expression as in definition (7) and the barrier functions B_i take the same expression as in relations (11) and (16).

The detailed expression of the mixed-form potential reads

$$\begin{aligned} V_{\mathrm{MIX}}(R) = &-\frac{1}{2}K_{\mathrm{A}}\ell^2\exp\left(-\frac{d^2(R,R_{\mathrm{d}})}{\ell^2}\right) \\ &-\frac{1}{2}d^2(R,R_{\mathrm{d}})\Bigg(K_{\mathrm{M}}\sum_i \log(e_{\mathrm{M},i}^{\top}R\,e_{\mathrm{BA}}-\cos\theta_{\mathrm{M},i}) \\ &+K_{\mathrm{F}}\sum_i \log(\cos\theta_{\mathrm{F},i}-e_{\mathrm{F},i}^{\top}R\,e_{\mathrm{BS}})\Bigg). \end{aligned} \tag{22}$$

The torque control component corresponding to the Riemannian gradient of such virtual potential may be determined by going through the same calculations shown in Section 3.2. The obtained expression $T_{\mathrm{MIX}}(R) := -R^{\top}\nabla_R V_{\mathrm{MIX}}(R)$ reads

$$\begin{aligned} T_{\mathrm{MIX}} = &-K_{\mathrm{A}}\exp\left(-\frac{d^2(R,R_{\mathrm{d}})}{\ell^2}\right)\mathrm{Log}(R_{\mathrm{d}}^{\top}R) \\ &+\Bigg(K_{\mathrm{M}}\sum_i \log(e_{\mathrm{M},i}^{\top}R\,e_{\mathrm{BA}}-\cos\theta_{\mathrm{M},i}) \\ &+K_{\mathrm{F}}\sum_i \log(\cos\theta_{\mathrm{F},i}-e_{\mathrm{F},i}^{\top}R\,e_{\mathrm{BS}})\Bigg)\mathrm{Log}(R_{\mathrm{d}}^{\top}R) \\ &+\frac{1}{2}d^2(R,R_{\mathrm{d}})\Bigg(\sum_i \frac{K_{\mathrm{M}}}{e_{\mathrm{M},i}^{\top}R\,e_{\mathrm{BA}}-\cos\theta_{\mathrm{M},i}}\sigma(R^{\top}e_{\mathrm{M},i}e_{\mathrm{BA}}^{\top}) \\ &+\sum_i \frac{K_{\mathrm{F}}}{e_{\mathrm{F},i}^{\top}R\,e_{\mathrm{BS}}-\cos\theta_{\mathrm{F},i}}\sigma(R^{\top}e_{\mathrm{F},i}e_{\mathrm{BS}}^{\top})\Bigg). \end{aligned} \tag{23}$$

With reference to the classical error-feedback control, it is worth noticing that the above expression appears as a weighted sum of the reorientation error $\mathrm{Log}(R_{\mathrm{d}}^{\top}R)$ and of a constraint-enforcing torque $\sum_i \frac{K_{\mathrm{M}}}{e_{\mathrm{M},i}^{\top}R\,e_{\mathrm{BA}}-\cos\theta_{\mathrm{M},i}}\sigma(R^{\top}e_{\mathrm{M},i}e_{\mathrm{BA}}^{\top}) + \sum_i \frac{K_{\mathrm{F}}}{\cos\theta_{\mathrm{F},i}-e_{\mathrm{F},i}^{\top}R\,e_{\mathrm{BS}}}\sigma(R^{\top}e_{\mathrm{F},i}e_{\mathrm{BS}}^{\top})$.

It is immediate to recognize that, at the sought equilibrium point $R=R_{\mathrm{d}}$, it holds that $V_{\mathrm{MIX}}(R_{\mathrm{d}}) = -\frac{1}{2}K_{\mathrm{A}}\ell^2$ and, more importantly, that $T_{\mathrm{MIX}}(R_{\mathrm{d}}) = 0$. Such approach hence overcomes the problem of non-zero tidal torque at equilibrium entailed by the approach presented in Section 3.2. The rightmost addendum in the virtual potential (22) may be interpreted as an additive repulsive potential *weighted* by an attractive potential increasing with the distance to the desired attitude which is able to fix the tidal-torque effect.

The most important difference to the potential function described in [6] is the presence of the sub-potential function A in the expression (22). A rationale for such choice is that, without an attractive sub-potential function, there would be no chance to balance the actions of the repulsive terms.

3.4. Relation with a navigation function

The barrier terms, that the above-discussed virtual potential functions are based on, may be recast in a different expression by exploiting

Table 2
Summary of the principal mathematical symbols introduced in Section 3.

Symbol	Type	Unit	Meaning
$R_{\rm i}$	SO(3)	–	Initial attitude of the spacecraft with respect to $\mathcal{F}_{\rm I}$
$R_{\rm d}$	SO(3)	–	Desired attitude of the spacecraft with respect to $\mathcal{F}_{\rm I}$
$e_{{\rm M},i}$	$\mathbb{R}^3$-versor	–	ith mandatory direction with respect to $\mathcal{F}_{\rm I}$
$\theta_{{\rm M},i}$	Angle	rad	Semi-aperture of the ith mandatory cone
$e_{{\rm F},j}$	$\mathbb{R}^3$-versor	–	jth forbidden direction with respect to $\mathcal{F}_{\rm I}$
$\theta_{{\rm F},j}$	Angle	rad	Semi-aperture of the jth mandatory cone
$e_{\rm BA}$, $e_{\rm BS}$	$\mathbb{R}^3$-versor	–	Boresight of antenna and sensor with respect to $\mathcal{F}_{\rm I}$
$K_{\rm f}$	Positive scalar	rad s/(kg m^2)	Artificial rotational friction constant
V	SO(3) $\to \mathbb{R}$	kg m^2/s^2	Artificial attractive–repulsive potential function
∇_R	Operator	–	Riemannian gradient in the rotation group SO(3)
$J_{\rm C}$	Positive scalar	kg m/s^2	Principal value of inertia of the spacecraft
A, B_k	SO(3) $\to \mathbb{R}$	kg m^2/s^2	Attractive and kth barrier-type components of a potential
d	SO(3) $\times$ SO(3) $\to \mathbb{R}$	–	Riemannian distance in the rotation group SO(3)
$K_{\rm A}$, ℓ	Positive scalar	kg m^2/s^2, –	Height and extent of the Gaussian attractive component
$K_{\rm M}$, $K_{\rm F}$	Positive scalar	kg m^2/s^2	Magnitudes of the mandatory and forbidden components
$T_{\rm ADD}$	$\mathfrak{so}(3)$	kg m^2/s^2	Control torque associated to the additive artificial potential
$T_{\rm MIX}$	$\mathfrak{so}(3)$	kg m^2/s^2	Control torque associated to mixed-type artificial potential

the properties of the natural logarithm. In fact, upon defining the total barrier potential term

$$B_{\rm T} := K_{\rm M} \sum_i \log(e_{{\rm M},i}^{\top} R\, e_{\rm BA} - \cos\theta_{{\rm M},i}) + K_{\rm F} \sum_i \log(\cos\theta_{{\rm F},i} - e_{{\rm F},i}^{\top} R\, e_{\rm BS}), \quad (24)$$

it is immediate to recognize that

$$\begin{aligned} B_{\rm T} &= \sum_i \log(e_{{\rm M},i}^{\top} R\, e_{\rm BA} - \cos\theta_{{\rm M},i})^{K_{\rm M}} + \sum_i \log(\cos\theta_{{\rm F},i} - e_{{\rm F},i}^{\top} R\, e_{\rm BS})^{K_{\rm F}} \\ &= \log\left(\prod_i (e_{{\rm M},i}^{\top} R\, e_{\rm BA} - \cos\theta_{{\rm M},i})^{K_{\rm M}} \prod_i (\cos\theta_{{\rm F},i} - e_{{\rm F},i}^{\top} R\, e_{\rm BS})^{K_{\rm F}} \right). \end{aligned} \quad (25)$$

It readily follows that

$$\exp(B_{\rm T}) = \prod_i \prod_j (e_{{\rm M},i}^{\top} R\, e_{\rm BA} - \cos\theta_{{\rm M},i})^{K_{\rm M}} (\cos\theta_{{\rm F},j} - e_{{\rm F},j}^{\top} R\, e_{\rm BS})^{K_{\rm F}}. \quad (26)$$

Hence the total barrier function may be regarded as a product of partial functions that are positive only in the permissible zones delimited by each barrier, a design strategy suggested in [27], where the weighting coefficients $K_{\rm M}$ and $K_{\rm F}$ play the role of order parameters.

3.5. Summary of the symbols introduced in Section 3

Within the present section a number of symbols were introduced. The type, measurement unit and meaning of the principal symbols introduced in the present section have been summarized in Table 2.

4. Results of numerical simulations

The present section illustrates and discusses the results of several numerical simulations performed on reorientation maneuvers. In all numerical simulations the stepsize was set to $h = 0.01$ s and the inertia coefficient took the value $J_{\rm C} = 144$ kg m^2. In addition, the initial angular speed Ω_0 was set to 0_3 (which denotes a null 3×3 matrix). In all numerical simulations the values of the coefficients of the potential functions, such as $K_{\rm A}$, $K_{\rm M}$, $K_{\rm F}$, and so forth, have been handcrafted by a trial-and-error process so as to achieve compelling results.

As a general note, within the present section all numerical data were expressed by no more than four decimal digits, whereas the actual computations by the computer codes were performed in maximum precision allowed by the computing platform.

4.1. Numerical simulations adapted from [6]

In order to test the reorientation strategy, we repeated numerical simulations adapted from [6] with two different potentials, namely, additive-potential and mixed-potential.

In these simulations, the spacecraft is assumed to be endowed with a radio antenna whose boresight axis is $e_{\rm BA} = [0\ 1\ 0]^{\top}$ and a telescope whose boresight axis is $e_{\rm BS} = [0\ 0\ 1]^{\top}$. In order to evaluate the performance of reorientation, we defined the following figure of merit, referred to as Reorientation Performance Indicator:

$$\text{RPI} := 100 \left(1 - \frac{d(R_{\rm a}, R_{\rm d})}{d(R_{\rm i}, R_{\rm d})} \right) \ (\%), \quad (27)$$

where $R_{\rm a} \in$ SO(3) represents the attitude actually achieved by the reorientation control algorithm in the given timespan of each experiment.

Table 3
Numerical data corresponding to the *Experiment 1*. The rotation matrices that represent attitudes are expressed in JPL quaternion notation for the sake of notation conciseness.

Description	Numerical value
Initial attitude $R_{\rm i}$	$(0.8385, 0.5062, -0.0043, 0.2017)$
Desired attitude $R_{\rm d}$	$(0.6603, -0.0907, 0.5925, 0.4525)$
Mandatory direction $e_{\rm M}$	$[0.8530\ \ -0.2653\ \ 0.4495]^{\top}$
Aperture of the mandatory cone $\theta_{\rm M}$	70 (deg)

Experiment 1: The first experiment consisted in simulating reorientation from an initial attitude, described by the matrix $R_{\rm i}$, to a desired attitude, described by the rotation matrix $R_{\rm d}$, in the presence of a mandatory-type zone, according to *Case 2* discussed in the paper [6]. The Table 3 shows the data pertaining to this simulation.

This reorientation problem was tackled by an additive-potential-based control algorithm as explained in Section 3.2. In this experiment, the potential and the associated torque read

$$\begin{cases} V_{\rm ADD}(R) = & -\frac{1}{2} K_{\rm A} \ell^2 \exp\left(-\frac{d^2(R_{\rm d}, R)}{\ell^2} \right) - K_{\rm M} \log(e_{\rm M}^{\top} R\, e_{\rm BA} - \cos\theta_{\rm M}), \\ T_{\rm ADD}(R) = & -K_{\rm A} \exp\left(-\frac{d^2(R_{\rm d}, R)}{\ell^2} \right) \text{Log}(R_{\rm d}^{\top} R) + \frac{K_{\rm M}}{e_{\rm M}^{\top} R\, e_{\rm BA} - \cos\theta_{\rm M}} \sigma(R^{\top} e_{\rm M} e_{\rm BA}^{\top}). \end{cases} \quad (28)$$

The numerical results were obtained upon setting $K_{\rm A} = 0.28\, J_{\rm C}$, $\ell = \sqrt{50}$, $K_{\rm f} = 1.4\, J_{\rm C}$, $K_{\rm M} = 10^{-5} J_{\rm C}$. Notice that the value of some of the constants was parameterized by the inertia coefficient $J_{\rm C}$ for convenience. The reorientation maneuver result achieved by the control algorithm, in terms of Reorientation Performance Indicator, in this experiment is RPI = 100%. The Fig. 1 illustrates the achieved results in terms of objective performances. The geodesic distance between the actual attitude and the desired attitude tends to zero and the value of the virtual potential tends to its target value during the timespan of the simulation.

A view of the achieved results in terms of 3D representation on the celestial sphere and of 2D cylindrical projection is provided in Fig. 2. (A review of 3D celestial-sphere representation and 2D cylindrical projection is proposed in B.) As it may be readily appreciated from this figure, the optimization-based control algorithm effectively attains the

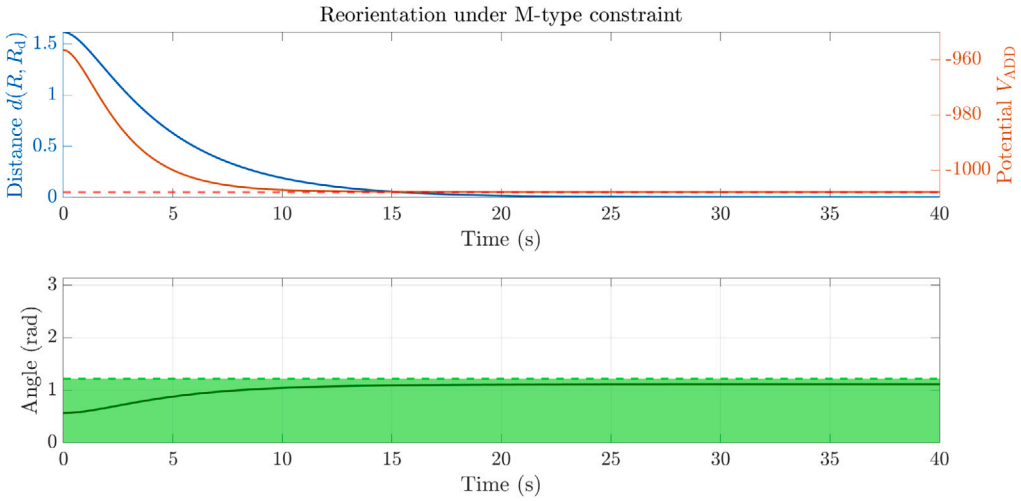

Fig. 1. Results obtained in the *Experiment 1* in terms of objective performance indexes. Top panel: Values of the distance between the actual attitude and the desired attitude, and value of the potential during reorientation; the dashed horizontal line represents the target value of the potential. Bottom panel: Angle between the boresight direction of the antenna and the mandatory direction; the green area represents the mandatory-type zone. (For interpretation of the references to color in this figure legend, the reader is referred to the web version of this article.)

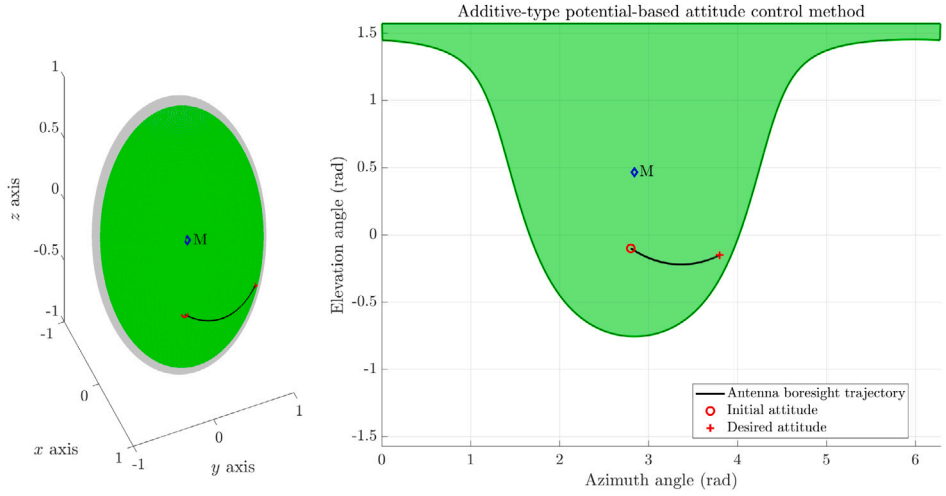

Fig. 2. Results obtained in the *Experiment 1* in terms of trajectory on the celestial sphere (left-hand panel) and 2D cylindrical projection (right-hand panel). The celestial sphere has unitary radius by convention and the axis carry no measurement unit. The slight distortion of the axes is merely a graphical side effect due to the chosen viewpoint. The green area represents the mandatory-type zone. A diamond mark represents the mandatory direction e_M. (For interpretation of the references to color in this figure legend, the reader is referred to the web version of this article.)

desired attitude while keeping the boresight of the antenna within the mandatory cone at all times.

The results shown in Fig. 2 may be compared with those illustrated in Fig. 14 of the paper [6]. In fact, the simulation data in Table 3 were handcrafted so as to reproduce the experiment proposed and discussed in Section VII.B of [6] as closely as possible. A direct comparison reveals that the novel control theory yields a shorter (non-wiggly) trajectory to achieve reorientation, having set the parameters in such a way that reorientation is completed within the same timespan as in [6].

We shall just mention that the same reorientation problem was tackled with the mixed-type potential-based control strategy that resulted in exactly the same trajectory.

Experiment 2: The second experiment consisted in simulating reorientation in the presence of four forbidden-type zones, according to *Case 1a* discussed in the paper [6]. The Table 4 shows the data pertaining to this simulation.

As a first attempt, such problem was tackled by an additive-potential-based control algorithm as explained in Section 3.2. In this case, the potential and the associated torque read

$$\begin{cases} V_{\mathrm{ADD}}(R) = & -\frac{1}{2}K_{\mathrm{A}}\ell^2\exp\left(-\frac{d^2(R_{\mathrm{d}},R)}{\ell^2}\right) - K_{\mathrm{F}}\log(\cos\theta_{\mathrm{F1}} - e_{\mathrm{F1}}^{\top}R\,e_{\mathrm{BS}}) \\ & - K_{\mathrm{F}}\log(\cos\theta_{\mathrm{F2}} - e_{\mathrm{F2}}^{\top}R\,e_{\mathrm{BS}}) - K_{\mathrm{F}}\log(\cos\theta_{\mathrm{F3}} - e_{\mathrm{F3}}^{\top}R\,e_{\mathrm{BS}}) \\ & - K_{\mathrm{F}}\log(\cos\theta_{\mathrm{F4}} - e_{\mathrm{F4}}^{\top}R\,e_{\mathrm{BS}}), \\ T_{\mathrm{ADD}}(R) = & -K_{\mathrm{A}}\exp\left(-\frac{d^2(R_{\mathrm{d}},R)}{\ell^2}\right)\mathrm{Log}(R_{\mathrm{d}}^{\top}R) + \frac{K_{\mathrm{F}}}{e_{\mathrm{F1}}^{\top}R\,e_{\mathrm{BS}}-\cos\theta_{\mathrm{F1}}}\sigma(R^{\top}e_{\mathrm{F1}}e_{\mathrm{BS}}^{\top}) \\ & + \frac{K_{\mathrm{F}}}{e_{\mathrm{F2}}^{\top}R\,e_{\mathrm{BS}}-\cos\theta_{\mathrm{F2}}}\sigma(R^{\top}e_{\mathrm{F2}}e_{\mathrm{BS}}^{\top}) + \frac{K_{\mathrm{F}}}{e_{\mathrm{F3}}^{\top}R\,e_{\mathrm{BS}}-\cos\theta_{\mathrm{F3}}}\sigma(R^{\top}e_{\mathrm{F3}}e_{\mathrm{BS}}^{\top}) \\ & + \frac{K_{\mathrm{F}}}{e_{\mathrm{F4}}^{\top}R\,e_{\mathrm{BS}}-\cos\theta_{\mathrm{F4}}}\sigma(R^{\top}e_{\mathrm{F4}}e_{\mathrm{BS}}^{\top}). \end{cases} \tag{29}$$

The numerical results obtained with an additive potential, where it was set $K_{\mathrm{A}} = 0.5\,J_{\mathrm{C}}$, $\ell = \sqrt{5}$, $K_{\mathrm{f}} = 1.5\,J_{\mathrm{C}}$, $K_{\mathrm{F}} = 0.035\,J_{\mathrm{C}}$, are illustrated in Fig. 3. The result achieved by the control algorithm in the given timeframe is RPI = 95.8%. As it may be readily appreciated from this figure, the optimization-based control algorithm attains the target value

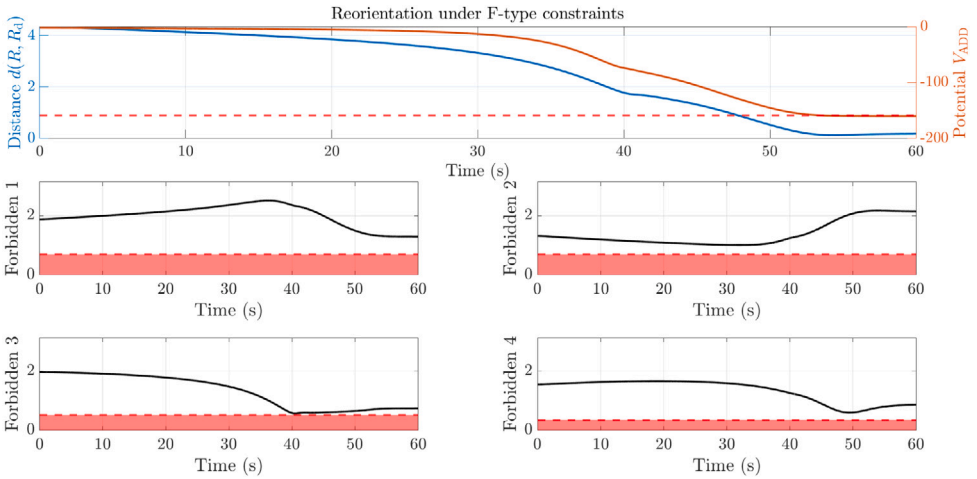

Fig. 3. Results obtained in the *Experiment 2*, tackled with an additive potential, in terms of objective performance indexes. Top panel: Values of the distance between the actual attitude and the desired attitude, and value of the potential during reorientation; the dashed line represents the target value of the potential. Lower panels: Angle between the boresight direction of the telescope and the forbidden directions (in radians); the red areas represent the forbidden-type zones. (For interpretation of the references to color in this figure legend, the reader is referred to the web version of this article.)

Table 4
Numerical data corresponding to the *Experiment 2*. The two rotation matrices are expressed in JPL quaternion notation for the sake of notation conciseness.

Description	Numerical value
Initial attitude R_i	$(0.6103, -0.4763, -0.1919, 0.6032)$
Desired attitude R_d	$(0.3844, 0.7966, 0.2665, 0.3830)$
Forbidden direction $e_{F,1}$	$[-0.1724\ \ 0.9256\ \ -0.3369]^\top$
Forbidden direction $e_{F,2}$	$[0\ \ -0.7071\ \ 0.7071]^\top$
Forbidden direction $e_{F,3}$	$[0.8532\ \ -0.4361\ \ -0.2861]^\top$
Forbidden direction $e_{F,4}$	$[0.1220\ \ 0.1399\ \ -0.9826]^\top$
Aperture of the first forbidden cone $\theta_{F,1}$	40 (deg)
Aperture of the second forbidden cone $\theta_{F,2}$	40 (deg)
Aperture of the third forbidden cone $\theta_{F,3}$	30 (deg)
Aperture of the fourth forbidden cone $\theta_{F,4}$	20 (deg)

Table 5
Numerical data corresponding to the *Experiment 3*. The rotation matrices representing initial and desired attitude are expressed in JPL quaternion notation for the sake of notation conciseness.

Description	Numerical value
Initial attitude R_i	$(0.7075, 0.4407, -0.2783, 0.4773)$
Desired attitude R_d	$(0.2898, 0.5406, 0.7840, 0.0948)$
Forbidden direction $e_{F,1}$	$[-0.1631\ \ 0.9864\ \ 0.0200]^\top$
Forbidden direction $e_{F,2}$	$[0\ \ -0.5733\ \ 0.8194]^\top$
Forbidden direction $e_{F,3}$	$[0.0673\ \ 0.4638\ \ -0.8834]^\top$
Forbidden direction $e_{F,4}$	$[0.8141\ \ -0.5487\ \ -0.1903]^\top$
Aperture of the first forbidden cone $\theta_{F,1}$	20 (deg)
Aperture of the second forbidden cone $\theta_{F,2}$	30 (deg)
Aperture of the third forbidden cone $\theta_{F,3}$	20 (deg)
Aperture of the fourth forbidden cone $\theta_{F,4}$	40 (deg)

of the potential function while keeping the boresight of the sensor away from the forbidden cones, although the distance to target does not reach a value sufficiently close to zero.

As a second attempt, such problem was tackled by a mixed-potential-based control algorithm as explained in Section 3.3. In this case, the potential and the associated torque read

$$\begin{cases} V_{MIX}(R) = & -\frac{1}{2}K_A\ell^2\exp\left(-\frac{d^2(R_d,R)}{\ell^2}\right) \\ & -\frac{1}{2}K_F d^2(R,R_d)(\log(\cos\theta_{F1} - e_{F1}^\top R\, e_{BS}) + \log(\cos\theta_{F2} - e_{F2}^\top R\, e_{BS}) \\ & \quad + \log(\cos\theta_{F3} - e_{F3}^\top R\, e_{BS}) + \log(\cos\theta_{F4} - e_{F4}^\top R\, e_{BS})), \\ T_{MIX}(R) = & -K_A\exp\left(-\frac{d^2(R_d,R)}{\ell^2}\right)\mathrm{Log}(R_d^\top R) \\ & + \frac{1}{2}d^2(R,R_d)\left(\frac{K_F}{e_{F1}^\top R\, e_{BS} - \cos\theta_{F1}}\sigma(R^\top e_{F1}e_{BS}^\top) + \frac{K_F}{e_{F2}^\top R\, e_{BS} - \cos\theta_{F2}}\sigma(R^\top e_{F2}e_{BS}^\top)\right. \\ & \quad \left. + \frac{K_F}{e_{F3}^\top R\, e_{BS} - \cos\theta_{F3}}\sigma(R^\top e_{F3}e_{BS}^\top) + \frac{K_F}{e_{F4}^\top R\, e_{BS} - \cos\theta_{F4}}\sigma(R^\top e_{F4}e_{BS}^\top)\right) \\ & + K_F(\log(\cos\theta_{F1} - e_{F1}^\top R\, e_{BS}) + \log(\cos\theta_{F2} - e_{F2}^\top R\, e_{BS}) \\ & \quad + \log(\cos\theta_{F3} - e_{F3}^\top R\, e_{BS}) + \log(\cos\theta_{F4} - e_{F4}^\top R\, e_{BS}))\mathrm{Log}(R_d^\top R), \end{cases} \tag{30}$$

The numerical results obtained with a mixed additive-multiplicative potential, where $K_A = 0.2\,J_C$, $\ell = \sqrt{50}$, $K_f = 2\,J_C$, $K_F = 0.028\,J_C$, are illustrated in Fig. 4. The result achieved by the control algorithm in the given timespan is RPI = 100%. As it may be readily appreciated from this figure, the optimization-based control algorithm attains the target value of the potential function while keeping the boresight of the sensor away from the forbidden cones.

An aerospace-oriented view of the achieved results is provided in Fig. 5. The results displayed in Fig. 5 may be put in comparison to the results shown in Fig. 9(a) of paper [6] since the simulation inputs in Table 4 are equivalent to the data in Table I (sub-table 'a') of the referenced paper. The trajectory traced by the telescope's boresight direction on the 2D cylindrical projection is not redundant although it looks a bit more wiggly than the one taken as reference, due to the actions of four 'repelling' directional obstacles. The devised control algorithm guides the boresight of the telescope toward correct reorientation by avoiding the bright portions of the celestial sphere.

Experiment 3: The third experiment concerning reorientation is of the same type of *Experiment 2* and corresponds to *Case 1b* discussed in the paper [6]. The reorientation data pertaining to this simulation are, however, different from those of *Experiment 2* and are listed in Table 5.

The problem was tackled by an additive-potential-based control algorithm as explained in Section 3.2. The values of the coefficients chosen in this experiment were $K_A = 0.45\,J_C$, $\ell = \sqrt{50}$, $K_f = 3\,J_C$ and $K_F = 10^{-4}J_C$.

The numerical results obtained through an additive potential are illustrated in Fig. 6. The optimization-based control algorithm effectively attains the minimum value of the potential function while keeping the boresight of the sensor away from the forbidden cones. In this experiment, the result achieved by the control algorithm in the given timespan, in terms of reorientation performance, is RPI = 100%.

An aerospace-oriented view of the achieved results is provided in Fig. 7. Even in this experiment, the optimization-based control algorithm effectively attains the desired attitude while keeping the boresight of the telescope away from the forbidden cone. In this experiment, the desired attitude of the telescope is near the border of the forbidden cone centered at F_1, nevertheless the barrier-type potential

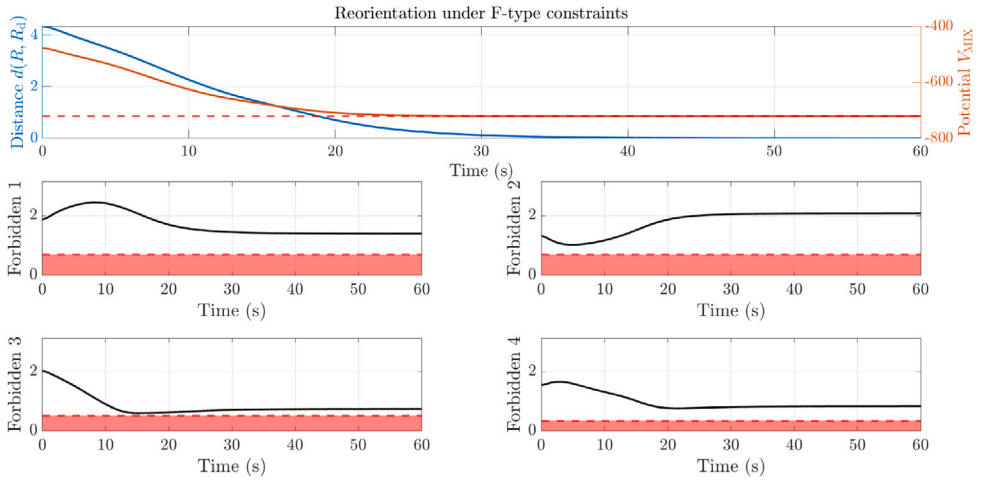

Fig. 4. Results obtained in the *Experiment 2*, tackled with a mixed additive-multiplicative potential, in terms of objective performance indexes. Top panel: Values of the distance between the actual attitude and the desired attitude, and value of the potential during reorientation; the dashed line represents the target value of the potential. Lower panels: Angle between the boresight direction of the telescope and the forbidden directions (in radians); the red areas represent the forbidden-type zones. (For interpretation of the references to color in this figure legend, the reader is referred to the web version of this article.)

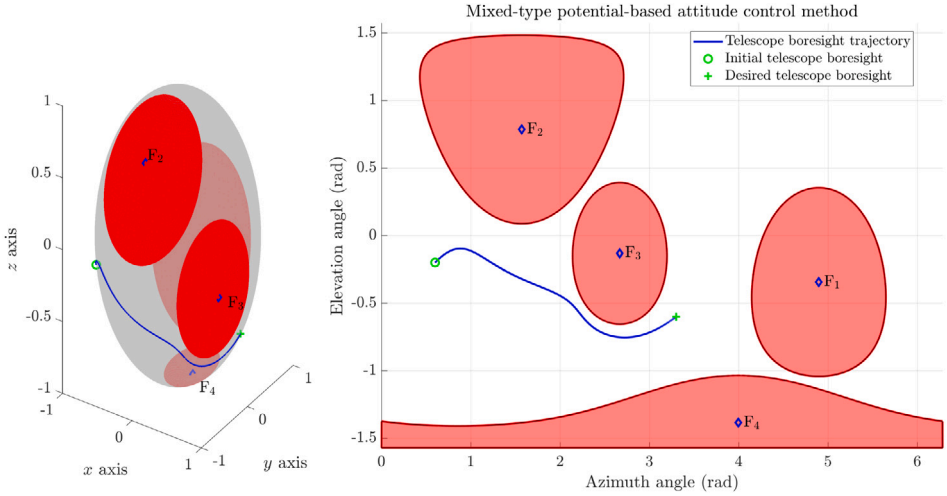

Fig. 5. Results obtained in the *Experiment 2* in terms of trajectory on the celestial sphere and 2D cylindrical projection, tackled through a mixed-type virtual potential. The celestial sphere has unitary radius by convention and the axis carry no measurement unit. The slight distortion of the axes is merely a graphical side effect due to the chosen viewpoint. The red areas represent the forbidden-type zones. The diamond marks represent the centers of the forbidden cones, identified by labels F_i, corresponding to the forbidden directions $e_{F,i}$, with $i = 1, 2, 3, 4$. (For interpretation of the references to color in this figure legend, the reader is referred to the web version of this article.)

keeps it away from such bright portion of the celestial sphere. Such result may be put in direct comparison to that displayed in Fig. 9(b) of Ref. [6]: The obtained trajectory in the azimuth/elevation space looks shorter than the reference one, especially in the first half.

We were able to obtain the same exact results by the control algorithm based on mixed additive-multiplicative virtual potential.

Experiment 4: The fourth experiment concerning reorientation is based on a mandatory-type zone and three forbidden-type zones and corresponds to *Case 3* discussed in the paper [6]. The Table 6 shows the reorientation data pertaining to this simulation.

As a first attempt, the problem was tackled by an additive-potential-based control algorithm as explained in Section 3.2. The values of the coefficients chosen in this experiment were $K_A = 0.045\, J_C$, $\ell = \sqrt{50}$, $K_f = 1.8\, J_C$, $K_M = 0.004\, J_C$ and $K_F = 0.006\, J_C$.

The results obtained with an additive potential are illustrated in Fig. 8. The optimization-based control algorithm effectively attains the target value of the potential function while keeping the boresight of the sensor away from the forbidden cones and the boresight of the antenna within the mandatory cone. However, the attained orientation does not match well the desired one, in fact the result achieved by the control algorithm in the given timespan is RPI = 32.3%.

Table 6
Numerical data corresponding to the *Experiment 4*. The rotation matrices are expressed in JPL quaternion notation for the sake of notation conciseness.

Description	Numerical value
Initial attitude R_i	(0.7140, 0.6370, 0.1300, −0.2600)
Desired attitude R_d	(−0.2300, −0.0800, −0.4910, 0.8400)
Mandatory direction e_M	$[0.8138 \;\; -0.5485 \;\; -0.1922]^\top$
Forbidden direction $e_{F,1}$	$[0 \;\; 1 \;\; 0]^\top$
Forbidden direction $e_{F,2}$	$[0 \;\; -0.8194 \;\; 0.5733]^\top$
Forbidden direction $e_{F,3}$	$[0.1221 \;\; 0.1391 \;\; -0.9827]^\top$
Aperture of mandatory cone θ_M	70 (deg)
Aperture of the first forbidden cone $\theta_{F,1}$	40 (deg)
Aperture of the second forbidden cone $\theta_{F,2}$	40 (deg)
Aperture of the third forbidden cone $\theta_{F,3}$	20 (deg)

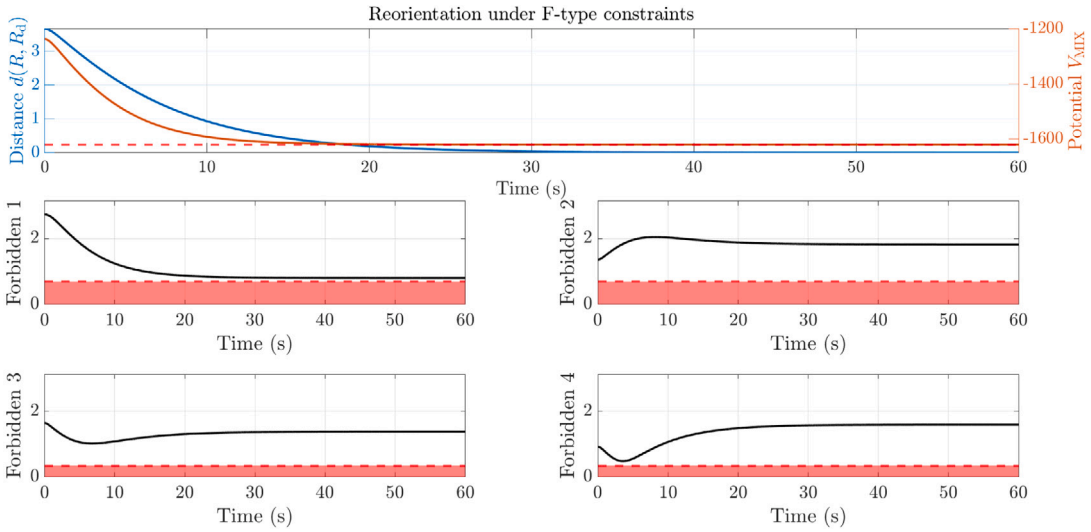

Fig. 6. Results obtained in the *Experiment 3*, in terms of objective performance indexes. Top panel: Values of the distance between the actual attitude and the desired attitude, and value of the potential during reorientation; the dashed line represents the target value of the potential. Lower panels: Angle between the boresight direction of the telescope and the forbidden directions (in radians); the red areas represent the forbidden-type zones. (For interpretation of the references to color in this figure legend, the reader is referred to the web version of this article.)

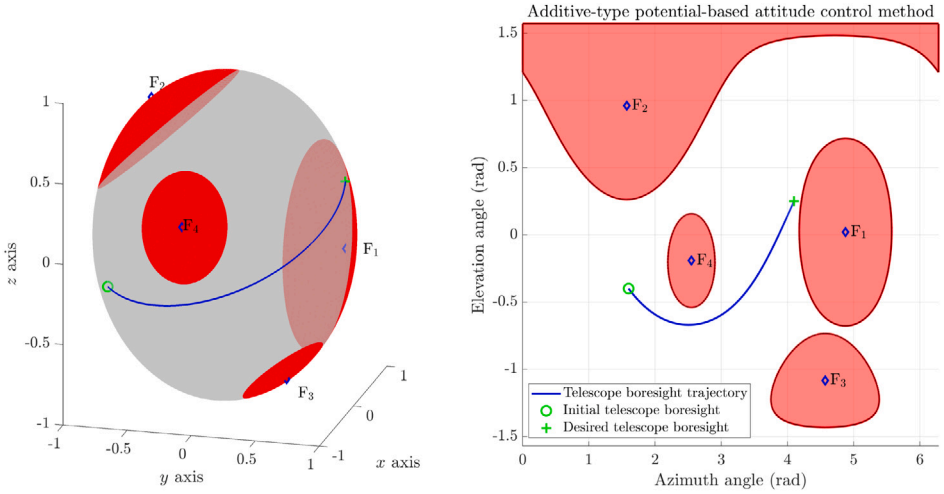

Fig. 7. Results obtained in the *Experiment 3* in terms of trajectory on the celestial sphere and 2D cylindrical projection. The red areas represent the forbidden-type zones. The celestial sphere has unitary radius by convention and the axis carry no measurement unit. The slight distortion of the axes is merely a graphical side effect due to the chosen viewpoint. The diamonds represent the centers of the forbidden cones, identified by labels F_i, corresponding to the forbidden directions $e_{F,i}$, with $i = 1, 2, 3, 4$. (For interpretation of the references to color in this figure legend, the reader is referred to the web version of this article.)

As a further attempt, the problem was tackled by a mixed additive-multiplicative potential-based approach as explained in Section 3.3. The values of the coefficients chosen in this experiment were $K_A = 0$, $K_f = 2.5\, J_C$, $K_M = 0.15\, J_C$ and $K_F = 0.012\, J_C$.

The numerical results obtained with a mixed additive-multiplicative potential are illustrated in Fig. 9. This experiment is the most challenging among those considered, because of the simultaneous presence of forbidden-type zones and a mandatory-type zone. In such further experiment, the result achieved by the control algorithm in the given timespan is RPI = 100%. The curves appear smooth and convergence to desired orientation appears steady.

An aerospace-oriented view of the achieved results is provided in Fig. 10. As it is readily appreciated form this figure, the forbidden cones and the mandatory cone are partially overlapping, which makes the reorientation endeavor more challenging than the previous cases. The same trajectories on a celestial sphere are illustrated in Fig. 11. The trajectory traced by the antenna's boresight direction on the 2D cylindrical projection is not redundant, namely, no such problems like unwinding and non-geodesic trajectories were encountered. Even in the present experiment, the obtained result may be compared to the corresponding result in paper [6] shown in Figure 15. A close examination of such results reveals that the trajectories produced by the proposed algorithm and the control algorithm in reference are quite different. In particular, the reorientation trajectory resulting from the proposed mixed additive-multiplicative potential, hence of the same kind of the one in [6], results shorter and free of redundancies. It

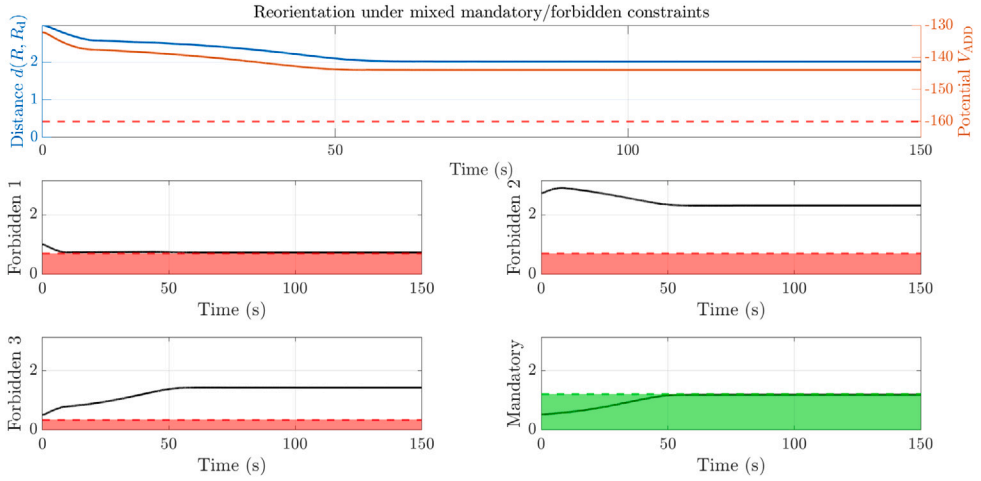

Fig. 8. Results obtained in the *Experiment 4*, tackled with a virtual additive potential, in terms of objective performance indexes. Top-left panel: values of the distance between the actual attitude and the desired attitude, and value of the potential during reorientation; the dashed line represents the target value of the potential pertaining to this experiment. Lower panels: Angle between the boresight direction of the telescope and each forbidden direction, as well as angle between the boresight direction of the antenna and the mandatory direction (in radians); the red areas represent the forbidden-type zones while the green area represents the mandatory-type zone. (For interpretation of the references to color in this figure legend, the reader is referred to the web version of this article.)

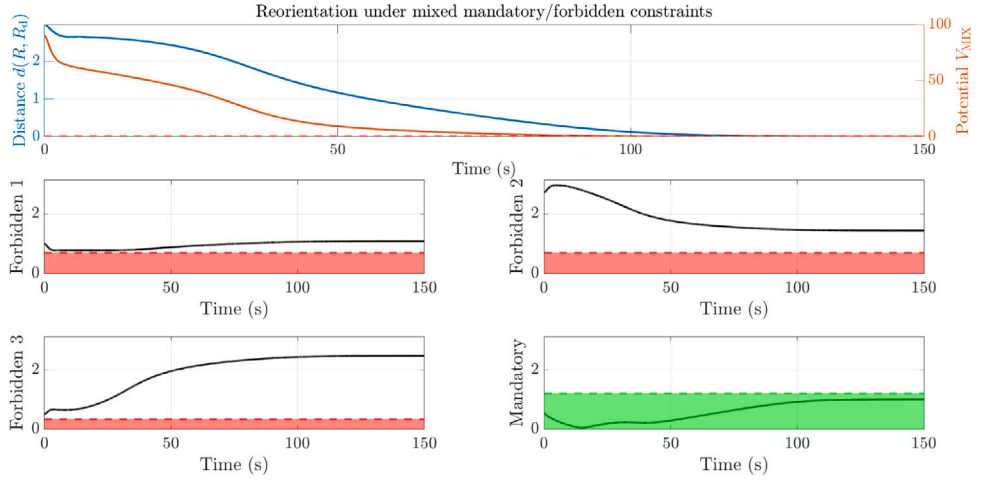

Fig. 9. Results obtained in the *Experiment 4*, tackled with a virtual additive-multiplicative potential, in terms of objective performance indexes. Top-left panel: values of the distance between the actual attitude and the desired attitude, and value of the potential during reorientation. Bottom-left and bottom-right panels: Angle between the boresight direction of the telescope and each forbidden direction, as well as angle between the boresight direction of the antenna and the mandatory direction; the red areas represent forbidden-type zones while the green area represents the mandatory-type zone. (For interpretation of the references to color in this figure legend, the reader is referred to the web version of this article.)

is quite interesting to notice that, in this experiment, the 'attractive' component of the potential is unnecessary, since it was set $K_A = 0$, whereby the role of 'attraction' is played by the multiplicative weight given by the squared distance function in the expression (22).

4.2. Numerical simulation on slanted antenna and telescope

In the present section, a further experiment is illustrated and commented on, which concerns reorientation under a mandatory constrain and three forbidden constraints as in *Experiment 4*, where, however, the antenna boresight and the telescope boresight are no longer perpendicular to one another.

Experiment 5: In this experiment, the boresight of the antenna and of the telescope were taken to be slanted of an angle of 30 deg each with respect to the y and z axes, respectively, so as to form an angle of 60 deg to each other. Their boresight versors were, in fact, taken as $e_{BA} = [0\ 0.9659\ 0.2588]^\top$ and $e_{BS} = [0\ 0.2588\ 0.9659]^\top$.

The reorientation problem was tackled by a mixed additive-multiplicative potential. The obtained result, in terms of objective performance indexes, are illustrated in Fig. 12. In such experiment, the result achieved by the control algorithm in the given timespan is RPI = 100%. The curves appear smooth and convergence to desired orientation appears steady. It is interesting to notice that the tackled problem turned out to be more challenging than the problem dealt with in *Experiment 4* since the desired orientation drives the antenna boresight very close to the rim of the mandatory cone.

A further illustration of the achieved results is provided in Fig. 13. As it is readily appreciated form this figure, the trajectory of the

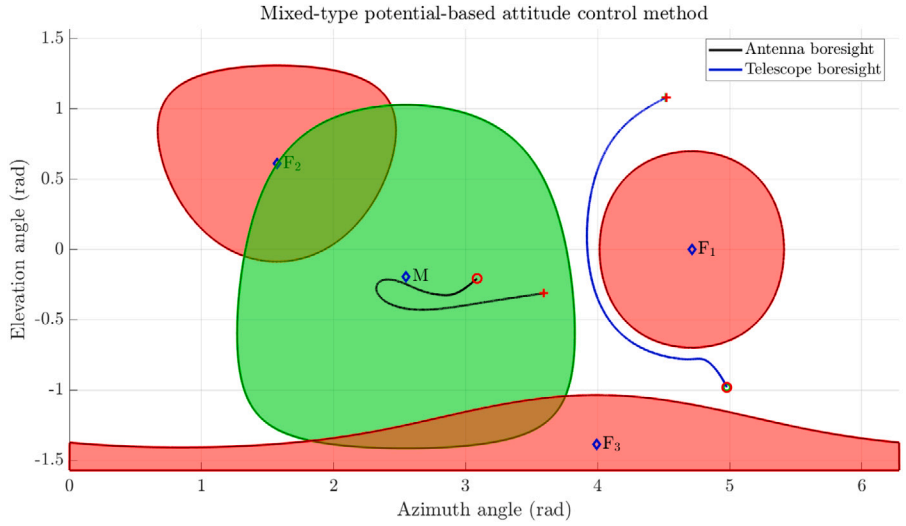

Fig. 10. Results obtained in the *Experiment 4*, tackled with a virtual additive-multiplicative potential, in terms of 2D cylindrical projection. The red areas represent the forbidden-type zones while the green area represents the mandatory-type zone. The diamonds represent the center of the mandatory cone, identified by the label M, as well as the centers of the forbidden cones, identified by labels F_i, corresponding to the forbidden directions $e_{\mathrm{F},i}$, with $i = 1, 2, 3$. A red open circle denotes the initial attitude, while the desired attitude – of both antenna and telescope boresight – is denoted by a red cross. (For interpretation of the references to color in this figure legend, the reader is referred to the web version of this article.)

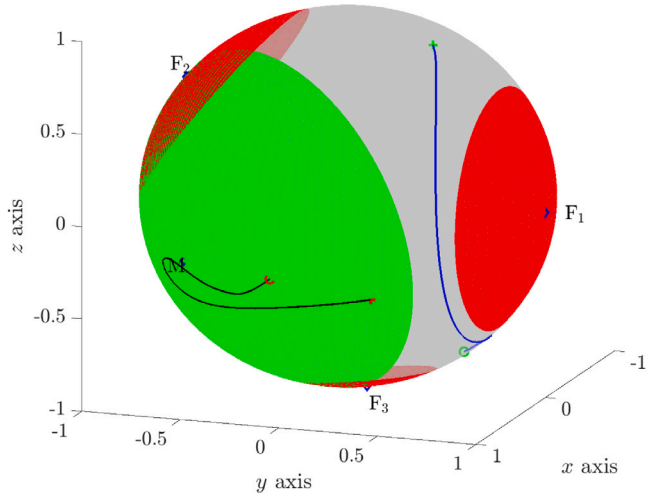

Fig. 11. Results obtained in the *Experiment 4*, tackled with a virtual additive-multiplicative potential, in terms of celestial-sphere representation. The red caps denote the forbidden-type zones while the green cap represents the mandatory-type zone. The celestial sphere has unitary radius by convention and the axis carry no measurement unit. The black line and the blue line carry the same meaning as in the companion Fig. 10. (For interpretation of the references to color in this figure legend, the reader is referred to the web version of this article.)

antenna boresight is completely enclosed within the mandatory area, while the trajectory of the sensor lies completely outside of each forbidden areas, while slightly entering the mandatory area, which is acceptable since such event does not violate any constraints. The trajectories of the boresight of the antenna and of the telescope on a celestial sphere are illustrated in Fig. 14. Again, in this experiment, the 'attractive' component of the potential was found experimentally to be unnecessary since the role of 'attraction' component of the potential was played by the multiplicative squared-distance weight in the expression (22).

4.3. Summary of the symbols introduced in Section 4

The type and meaning of the principal symbol and acronym used within the present section have been summarized in Table 7.

5. Conclusion

The aim of the present research endeavor was to propose a framework to model, simulate and control a small unmanned spacecraft, orbiting in close proximity of a space station, through Lie-group theory. In particular, automated reorientation of an unmanned under directional constraints has been tackled and simulated numerically.

The main theoretical instrument utilized in the present research is that of virtual attractive–repulsive potential. In fact, a physical object moves in a force field derived as anti-gradient of a potential function which embodies localized information about the spacecraft to be guided and the surrounding environment. Concerns raised in the scientific literature that the complexity of tasks that can be tackled by means of virtual potential is limited, because of local minima in the potential function [24] which may lead a controlled object to a stable configuration different from the intended goal, was debunked. In fact, it has been shown, even by the present contribution, that virtual-potential-based control, if properly designed and tuned, shows ability to lead to compelling results under reasonable tolerance levels.

A distinguishing feature of the present endeavor was that, unlikely most research papers in the area that invoke the use of coordinates or quaternions, the mathematical model of the roto-translational motion of a spacecraft as well as the design of control fields were written in a coordinate-free Lie-group-type fashion.

Several numerical simulations, aimed at complementing the theoretical developments, were discussed to illustrate the achieved progress and to guide the reader though a series of evaluations. Such evaluation stages were aimed at establishing which control strategy, among several possible combinations, appears to be the most convenient one. As a conclusive evaluation on the numerical simulations just illustrated, the attitude control method based on mixed additive-multiplicative potential proved more reliable as it always led to convergence to the

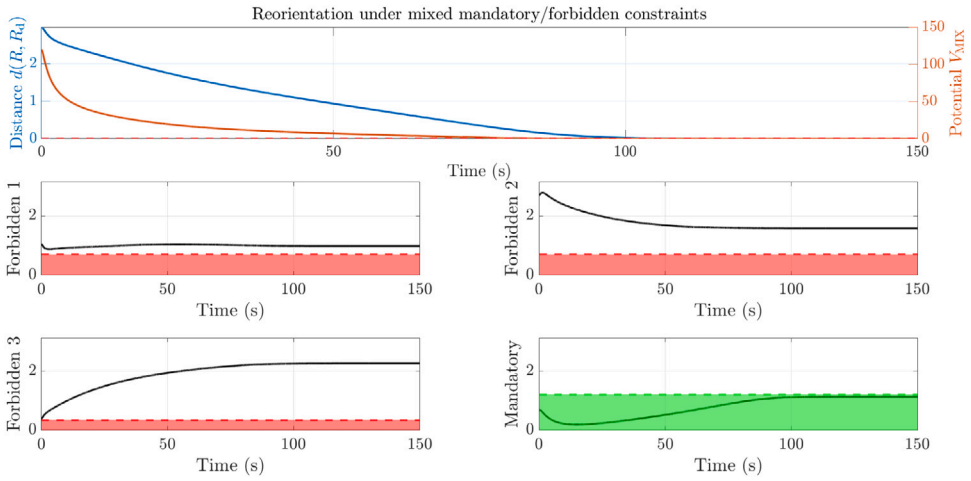

Fig. 12. Results obtained in the *Experiment 5*, tackled with a virtual additive-multiplicative potential, in terms of objective performance indexes. Top-left panel: values of the distance between the actual attitude and the desired attitude, and value of the potential during reorientation. Bottom-left and bottom-right panels: Angle between the boresight direction of the telescope and each forbidden direction, as well as angle between the boresight direction of the antenna and the mandatory direction; the red areas represent forbidden-type zones while the green area represents the mandatory-type zone. (For interpretation of the references to color in this figure legend, the reader is referred to the web version of this article.)

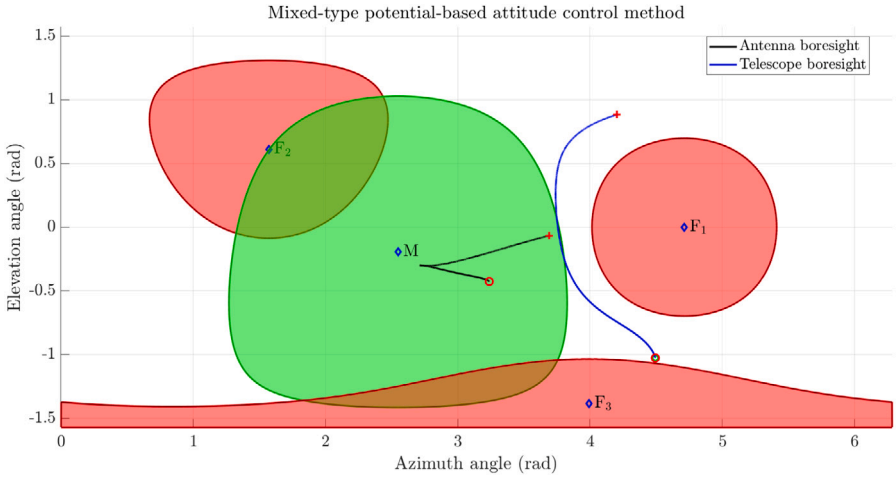

Fig. 13. Results obtained in the *Experiment 5*, tackled with a virtual additive-multiplicative potential, in terms of 2D cylindrical projection. The red areas represent the forbidden-type zones while the green area represents the mandatory-type zone. The diamonds represent the center of the mandatory cone, identified by the label M, as well as the centers of the forbidden cones, identified by labels F_i, corresponding to the forbidden directions $e_{\mathrm{F},i}$, with $i = 1, 2, 3$. A red open circle denotes the initial attitude, while the desired attitude – of both antenna and telescope boresight – is denoted by a red cross. (For interpretation of the references to color in this figure legend, the reader is referred to the web version of this article.)

Table 7
Summary of the principal mathematical symbol and acronym used in Section 4.

Symbol	Type	Meaning
R_a	SO(3)	Attitude of the spacecraft actually achieved in reference frame $\mathcal{F}_I$
RPI	Percentage	Performance indicator in a re-orientation maneuver

desired attitude, as long as the coefficients of attractive and repulsive terms and of the braking term are properly tuned.

An aspect to remark is that the discussed control strategies are able to guide a spacecraft through reorientation along minimal trajectories yet preventing oscillations. We shall remark that prevention of excessive oscillations in the control fields is of primary importance since oscillations are responsible for wear and tear of actuators (such as motor shafts in the reaction wheels) hence reducing dramatically their lifespan. As it emerges from the numerical simulation, re-orientation may be achieved in a relatively short timespan (less than 3 min in all experiments considered).

An aspect to pay attention to is the effect of repulsive fields far away from the obstacles, which may drive a spacecraft slightly off-track with respect to the intended target (referred to as 'tidal effect'). Such

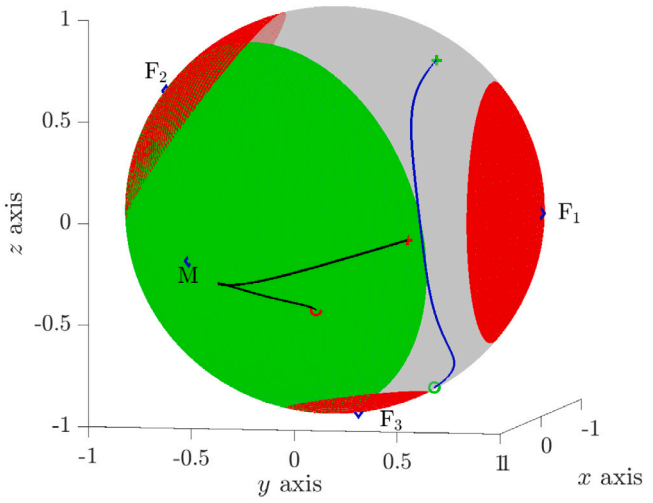

Fig. 14. Results obtained in the *Experiment 5*, tackled with a virtual additive-multiplicative potential, in terms of celestial-sphere representation. The red caps denote the forbidden-type zones while the green cap represents the mandatory-type zone. The celestial sphere has unitary radius by convention and the axis carry no measurement unit. The black line and the blue line carry the same meaning as in the companion Fig. 13. (For interpretation of the references to color in this figure legend, the reader is referred to the web version of this article.)

problem has been dealt with by tuning the constant parameters in the virtual potential function and in the control algorithm, although a hard-limiting strategy would perhaps prove more effective as it would cut off completely the repulsive fields whenever sufficiently far from their source.

Declaration of competing interest

The authors declare that they have no known competing financial interests or personal relationships that could have appeared to influence the work reported in this paper.

Acknowledgments

The authors would like to gratefully thank Prof. Toshihisa Tanaka (Tokyo University of Agriculture and Technology — TUAT, Japan) for hosting them at the Department of Electrical and Electronic Engineering of the TUAT (Koganei campus) during March–May, 2023. The authors FR, LS and ES were supported by a grant from the *Campus-World* internship programme of the Università Politecnica delle Marche (Italy).

Appendix A. On the unit-quaternion to rotation-matrix conversion precision

In a computer code, a unit quaternion denotes a point on a 4D hypersphere S^3 and a 3D rotation matrix denotes an element on the special orthogonal group SO(3) up to machine precision. While a rotation matrix is seldom expressed directly through its numerical entries, a quaternion often is. When the entries of a quaternion are describe by a *limited* number of digits, e.g. by four decimal digits, its conversion to a rotation matrix does not result in a true rotation. The conversion of a quaternion $[q_i\ q_j\ q_k\ q_0]^\top$ to a rotation matrix R may be expressed as [28]

$$\tilde{R} = \begin{bmatrix} 1-2(q_j^2+q_k^2) & 2(q_iq_j-q_kq_0) & 2(q_iq_k+q_jq_0) \\ 2(q_iq_j+q_kq_0) & 1-2(q_i^2+q_k^2) & 2(q_jq_k-q_iq_0) \\ 2(q_iq_k-q_jq_0) & 2(q_jq_k+q_iq_0) & 1-2(q_i^2+q_j^2) \end{bmatrix},$$

where q_o denotes the real part of the quaternion (in JPL notation). To fix non-unitarity, it is sensible to perform a projection to the SO(3) group based on singular value decomposition (SVD), namely

$$UDV^\top = \tilde{R},\ R := UV^\top,$$

where U, V denote the orthogonal factors of the SVD. The resulting matrix R is orthogonal up to machine precision.

Appendix B. A short review of 3D celestial sphere and 2D cylindrical representations

In the present instance, cylindrical coordinates are an instance of spherical coordinates where the radius variable is neglected since it does not carry any information (being constant).

More specifically, let us assume a unit vector $e \in \mathrm{S}^2$ pointing toward a given direction in the celestial sphere S^2 has coordinates $[e_\mathrm{x}\ e_\mathrm{y}\ e_\mathrm{z}]^\top$ such that $e_\mathrm{x}^2+e_\mathrm{y}^2+e_\mathrm{z}^2 = 1$. The azimuth and elevation are then calculated by the formulas:

$$\text{Azimuth} = \mathrm{atan}_2(e_\mathrm{y}, e_\mathrm{x}),\ \text{Elevation} = \mathrm{atan}_2\left(e_\mathrm{z}, \sqrt{e_\mathrm{x}^2+e_\mathrm{y}^2}\right),$$

where atan_2 denotes the 2-argument arc-tangent function, azimuth and elevation are expressed in radians.

In the present endeavor, a unit vector $e \in \mathrm{S}^2$ represents the boresight of either a communication antenna or an observation telescope. Let us denote, as in the main text, by $e_\mathrm{BA} \in \mathrm{S}^2$ the boresight direction of the communication device referred to the frame $\mathcal{F}_\mathrm{C}$, by $e_\mathrm{BS} \in \mathrm{S}^2$ the boresight direction of the sensor referred to the spacecraft-fixed frame $\mathcal{F}_\mathrm{C}$, and by $R(t) \in \mathrm{SO}(3)$ the instantaneous attitude-indicator matrix that describes the orientation of the spacecraft in the inertial reference frame $\mathcal{F}_\mathrm{I}$. Then, we might set either $e(t) = R(t)e_\mathrm{BA}$ or $e(t) = R(t)e_\mathrm{BS}$, depending on which device's trajectory we seek to display by either a celestial-sphere or a cylindrical-projection representation.

References

[1] D. Hill, Mission update: Voyager 2 communications pause, 2023, Article date: July 28, 2023, https://blogs.nasa.gov/sunspot/2023/07/28/mission-update-voyager-2-communications-pause/.
[2] I. Lopez, C.R. McInnes, Autonomous rendezvous using artificial potential function guidance, J. Guid. Control Dyn. 18 (2) (1995) 237–241, http://dx.doi.org/10.2514/3.21375.
[3] C.R. McInnes, Large angle slew maneuvers with autonomous sun vector avoidance, J. Guid. Control Dyn. 17 (4) (1994) 875–877, http://dx.doi.org/10.2514/3.21283.
[4] Q. Hu, B. Chi, M.R. Akella, Anti-unwinding attitude control of spacecraft with forbidden pointing constraints, J. Guid. Control Dyn. 42 (4) (2019) 822–835, http://dx.doi.org/10.2514/1.G003606.
[5] H.B. Hablani, Attitude commands avoiding bright objects and maintaining communication with ground station, J. Guid. Control Dyn. 22 (6) (1999) 759–767, http://dx.doi.org/10.2514/2.4469.
[6] U. Lee, M. Mesbahi, Feedback control for spacecraft reorientation under attitude constraints via convex potentials, IEEE Trans. Aerosp. Electron. Syst. 50 (4) (2014) 2578–2592, http://dx.doi.org/10.1109/TAES.2014.120240.
[7] R.E. Roberson, R. Schwertassek, Dynamics of Multibody Systems, Springer-Verlag Berlin Heidelberg, 1988.
[8] H. Cheng, K.C. Gupta, An historical note on finite rotations, J. Appl. Mech. 56 (1) (1989) 139–145, http://dx.doi.org/10.1115/1.3176034.
[9] S. Fiori, Model formulation over Lie groups and numerical methods to simulate the motion of gyrostats and quadrotors, Mathematics 7 (10) (2019) http://dx.doi.org/10.3390/math7100935.
[10] S. Fiori, I. Cervigni, M. Ippoliti, C. Menotta, Extension of a PID control theory to Lie groups applied to synchronising satellites and drones, IET Control Theory Appl. 14 (2020) 2628–2642.
[11] S. Fiori, L. Del Rossi, Minimal control effort and time Lie-group synchronisation design based on proportional-derivative control, Internat. J. Control (1) (2022) 138–150, http://dx.doi.org/10.1080/00207179.2020.1780474.
[12] J.L. Baxter, E.K. Burke, J.M. Garibaldi, M. Norman, Multi-robot search and rescue: A potential field based approach, in: S.C. Mukhopadhyay, G.S. Gupta (Eds.), Autonomous Robots and Agents, Springer Berlin Heidelberg, Berlin, Heidelberg, 2007, pp. 9–16, http://dx.doi.org/10.1007/978-3-540-73424-6_2.
[13] I. Kamon, E. Rimon, E. Rivlin, TangentBug: A range-sensor-based navigation algorithm, Int. J. Robot. Res. 17 (9) (1998) 934–953, http://dx.doi.org/10.1177/027836499801700903.

[14] D. Koditschek, E. Rimon, Robot navigation functions on manifolds with boundary, Adv. Appl. Math. 11 (4) (1990) 412–442.
[15] E. Leonard, E. Fiorelli, Virtual leaders, artificial potentials and coordinated control of groups, in: Proceedings of the 40th IEEE Conference on Decision and Control, 2001, pp. 2968–2973.
[16] Y. Rasekhipour, A. Khajepour, S. Chen, B. Litkouhi, A potential field-based model predictive path-planning controller for autonomous road vehicles, IEEE Trans. Intell. Transp. Syst. 18 (5) (2017) 1255–1267, http://dx.doi.org/10.1109/TITS.2016.2604240.
[17] S. Shimoda, Y. Kuroda, K. Iagnemma, Potential field navigation of high speed unmanned ground vehicles on uneven terrain, in: Proceedings of the 2005 IEEE International Conference on Robotics and Automation, 2005, pp. 2828–2833, http://dx.doi.org/10.1109/ROBOT.2005.1570542.
[18] B. Nguyen, Y.-L. Chuang, D. Tung, C. Hsieh, Z. Jin, L. Shi, D. Marthaler, A. Bertozzi, R. Murray, Virtual attractive-repulsive potentials for cooperative control of second order dynamic vehicles on the caltech MVWT, in: Proceedings of the 2005 American Control Conference, Portland, OR, USA, 2005, pp. 1084–1089.
[19] S. Fiori, L. Bigelli, F. Polenta, Lie-group type quadcopter control design by dynamics replacement and the virtual attractive-repulsive potentials theory, Mathematics 10 (7) (2022) 1104, http://dx.doi.org/10.3390/math10071104.
[20] N. Bloise, E. Capello, M. Dentis, E. Punta, Obstacle avoidance with potential field applied to a rendezvous maneuver, Appl. Sci. 7 (10) (2017) http://dx.doi.org/10.3390/app7101042.
[21] A. Bloch, P. Krishnaprasad, J. Marsden, G. de Alvarez, Stabilization of rigid body dynamics by internal and external torques, Automatica 28 (4) (1992) 745–756, http://dx.doi.org/10.1016/0005-1098(92)90034-D.
[22] D. Schneider, Non-holonomic Euler-poincaré equations and stability in Chaplygin's sphere, Dyn. Syst. 17 (2) (2002) 87–130, http://dx.doi.org/10.1080/02681110110112852.
[23] S. Fiori, Manifold calculus in system theory and control – fundamentals and first-order systems, Symmetry 13 (11) (2021) 2092, http://dx.doi.org/10.3390/sym13112092.
[24] O. Khatib, Real-time obstacle avoidance for manipulators and mobile robots, Int. J. Robot. Res. 5 (1) (1986) 90–98, http://dx.doi.org/10.1177/027836498600500106.
[25] S. Fiori, Manifold calculus in system theory and control – second order structures and systems, Symmetry 14 (6) (2022) 1144, http://dx.doi.org/10.3390/sym14061144.
[26] R.S. Chandrasekaran, L.J. Colombo, M. Camarinha, R. Banavar, A. Bloch, Variational collision and obstacle avoidance of multi-agent systems on Riemannian manifolds, in: 2020 European Control Conference, ECC, 2020, pp. 1689–1694, http://dx.doi.org/10.23919/ECC51009.2020.9143986.
[27] S. Paternain, D.E. Koditschek, A. Ribeiro, Navigation functions for convex potentials in a space with convex obstacles, IEEE Trans. Automat. Control 63 (9) (2018) 2944–2959, http://dx.doi.org/10.1109/TAC.2017.2775046.
[28] S. Sarabandi, F. Thomas, Accurate computation of quaternions from rotation matrices, in: J. Lenarcic, V. Parenti-Castelli (Eds.), Advances in Robot Kinematics 2018, Springer International Publishing, Cham, 2019, pp. 39–46.